UNIVERSITÀ DEGLI STUDI DI PADOVA

Department of
Civil, Environmental, and Architectural Engineering
Environment and Sustainability Program

Master Thesis

Peridynamics Modeling of Land Subsidence and Earth Fissure Due to Groundwater Extraction in the Picacho Basin, Arizona

Xi Tang

(2071537)

Supervisor
Prof. Eng. Pietro Teatini
Department of Civil, Environmental and Architectural Engineering,
University of Padova

Co-Supervisor
Dr. Miao Ye
Capital Normal University, Beijing

Academic Year 2023/2024

Acknowledgements

The completion of this thesis has become possible under the most professional guidance from Prof. Eng. Pietro Teatini of the Civil, Environmental and Architectural Engineering Department of University of Padova. Many of the ideas were inspired during the countless meetings and discussions between the professor and the author. The author is hereby giving his deepest gratefulness for the devotion in time and in patience from Prof. Eng. Pietro Teatini.

The author is also expressing his greatest thankfulness to Dr. Miao Ye of Captial Normal University, Beijing. She has provided the author access to pertinent unpublished information, and the supports are so crucial that, without her, the numerical modelling system would not have been possible to build.

Abstract

The problems of land subsidence and earth fissures have become two of the most widespread geohazard on the world. Although the Finite Element (FE) method has been widely applied to model land subsidence in the real case studies, its limitations in earth fissures simulation have become a bottleneck for further scientific researches. The current thesis adopted a newly developed modeling system based on Peridynamics. This approach is free from any limitation in classical continuum theory. Several mechanisms responsible for land subsidence and earth fissures are introduced, and a short review of the Peridynamics theory is also included in this thesis. Since the applicability and accuracy of the Peridynamics modeling framework in geomechanics is still unclear due to lack of practical applications into real cases, the current thesis initially compares the outcomes of Peridynamics with those obtained from an FE simulator on a simple case study. In a second phase, the Peridynamics simulator is used to investigate a real case study, i.e. a portion of the Picacho Basin, Arizona, US, where land subsidence and earth fissures due to groundwater extraction were recorded and investigated back in 1980s. Demonstrations of the capability of this approach are made by comparing land subsidence and earth fissures as obtained by the model and measured in the field. The comparison provides a satisfactory response. It can be concluded that the new Peridynamics modeling framework represents a powerful tool to predict land subsidence and earth fissures associated with overexploitation of complex aquifer systems.

Contents

List of Figures

Chapter 1

Introduction

Before the development of human society, land subsidence and earth fissures were predominantly natural processes driven by factors such as the natural consolidation of alluvial soils and tectonics. However, since the onset of the Industrial Revolution, rapid growth in population and industrial activities has significantly increased the demand for water, resulting in a continuous decline in groundwater levels. This marked a shift in the primary causes of land subsidence and earth fissures from natural geological processes to anthropogenic activities. Today, instances of land subsidence and earth fissures induced by excessive groundwater extraction are well documented and occur in regions across the world.

In Indonesia, Jakarta is experiencing one of the most severe episodes of land subsidence in its history, induced primarily by extensive groundwater extraction [1]. The situation has become so critical that the authorities have proposed relocating the capital from Java Island to Borneo Island to mitigate the associated risks. In China, excessive groundwater withdrawal has been identified as the primary cause of earth fissures and land subsidence in the Suzhou, Wuxi, and Changzhou regions, particularly in areas where the subsurface is characterized by the presence of buried bedrock ridges [2]. Similarly, in Japan, excessive groundwater pumping during the dry season leads to depletion of subsurface water, triggering land subsidence due to consolidation of the underlying clay layers. This has caused significant structural damage to thousands of private apartments and public infrastructure, including canals, levees, and bridges [3].

The impacts of land subsidence and earth fissures can be devastating. They result in a permanent reduction in the storage capacity of the aquifer system, cause significant damage to buildings and civil infrastructures, and increase the vulnerability to flooding. In the coming decades, the demand for groundwater extraction is expected to increase further, driven by economic growth in many regions. Consequently, it is imperative to develop robust simulators capable of predicting these geohazards. Such systems would enable sustainable groundwater management, allowing the fulfillment of water demands while minimizing damage to infrastructures and ensuring public safety.

One of the most advanced geomechanical approaches currently available for simulating land subsidence is the Finite Element Method (FEM). This approach involves reconstructing the study area by transforming realistic features into a mesh structure, where nodes and elements interact based on partial differential equations of equilibrium. However, challenges arise when dealing with spatial discontinuities, such as cracks. For example, crack formation introduces discontinuities that do not align with the initial mesh structure, necessitating complex remeshing techniques to adjust the mesh as the crack propagates. This process is computationally intensive and adds significant numerical complexity. In addition, cracks create stress concentrations at their tips, often resulting in mathematically infinite stress values, quantities that lack physical meaning and complicate the modeling process further. Although methods such as incorporating Interface Elements, also known as the Extended Finite Element Method (XFEM), provide a means to address this issue, challenges persist when dealing with multiple cracks within a model. Instability can arise during re-meshing or in regions with high stress gradients, making it difficult to achieve reliable convergence. These complexities highlight the limitations of current approaches and underscore the need for further advancements in computational techniques to improve the stability and accuracy of

such simulations.

To address the challenges associated with the Finite Element Method, this thesis adopts a novel 3D numerical modeling system based on Peridynamics. The study aims to demonstrate the capability of this approach in simulating land subsidence and earth fissures, as well as its applicability across various geomechanical structures. The Peridynamics model used in this research was developed by Dr. Miao at Capital Normal University (Beijing) [4], and is based on the Ordinary State-Based Peridynamics theory proposed by Silling [5]. This modeling approach provides the ability to directly apply its fundamental equations to discontinuities, such as cracks [5]. Unlike the classical theory of solid mechanics, which relies on partial differential equations (PDEs), the Peridynamics framework replaces these with integral or integro-differential equations, allowing for a more natural representation of discontinuities [6].

To implement the Peridynamics theory and demonstrate its effectiveness and efficiency, this thesis adopts a case study of land subsidence and earth fissures in the Picacho Basin, Arizona, as the target for Peridynamics modeling. A crucial step in this process is the digitization of field data observed and recorded in previously published work [7], which will serve as input parameters for the model. These input parameters, as described in the referenced study, include, but are not limited to, the inferred subsurface profile, the extent of the decline in the water table, and the soil layers along with their densities in the Picacho Basin.

Once the model is constructed, a comparison is made between the simulation results from the Peridynamics model and the actual field observations of land subsidence and earth fissures in the study area. Since certain soil parameters, such as Young's modulus, cohesion, and internal friction angles, remain unknown, a trial-and-error approach is employed to iteratively adjust the assumed parameters. This iterative process aims to align the modeled results as closely as possible with the observed data, thereby refining the model's accuracy and demonstrating its applicability to real-world scenarios.

Before the modeling application to the Picacho Basin, the Peridynamics simulator is applied to two simplified models and validated against the outcomes of a Finite Element geomechanical model (FEM). As FEM is a well-established and widely recognized local continuum theory, comparing its results with those generated by the Peridynamics model provides a valuable benchmark. This comparison aims to further validate the accuracy and reliability of the Peridynamics modeling approach by demonstrating its consistency with results obtained from the traditional FEM framework.

The present thesis is organized as follows: Chapter 2 focuses on the characteristics of the study area, including its geographic location, climatic conditions, and subsurface layer compositions. Chapter 3 provides a detailed explanation of the mechanisms behind land subsidence and earth fissures, along with an overview of the Peridynamics framework. Chapter 4 introduces the implementation of the Peridynamics model in Python, including the setup procedures and the workflow for constructing the model. Chapter 5 presents results and discussion, featuring comparisons between Peridynamics and classical modeling methods. Chapter 6 concludes the thesis by summarizing the key findings derived from the research.

Chapter 2

Study Area

2.1 The Picacho Basin

Located roughly at the latitude from 111°50' to 111°15' and the longitude from 32°35' to 33°10', the Piscacho Basin occupies an area of about 2331 km^2. It is a structural basin in the Basin and Range Lowland Water province of Arizona [8]. This basin is defined by hydrologic boundaries that approximate the extent of the primary aquifer. Basically, the boundary is mainly formed by impermeable crystalline rock, which has restricted the flow of ground water and the mountains surrounded. These surrounding mountains ranging less than 1525 m above sea level. At the east edge of the basin, there are Picacho Mountains and Picacho Peak. The Silverbell, Sawtooth, and Silver Reef Mountains are located in the south and southwest corner of the basin. The west edge of the basin are the Casa Grande Mountains and the Sacaton Mountains. In the north boundary, it is formed by the Santan Mountains and the Gila River, where the Tortilla Mountains are located at the northeast extent of the basin. Figure 2.1a shows the basin domain indicated by a dark gray color within the state of Arizona, while Figure 2.1b is the zoom-in view of the Picacho Basin.

The Gila River, which flows along the northern side of the basin, is the primary stream in the area. Historically, before the development of surface water supplies, the Gila River flowed intermittently, which meant that it maintained flow for extended periods of the year or potentially year-round throughout the study area. In modern times, river flow is partially regulated by water releases from upstream reservoirs and by diversions at the Ashurst-Hayden Dam, located in the northeast corner of the basin. Other streams, such as the Santa Cruz River and McClellan Wash, typically flow only in response to local rainfall. In the western part of the basin, these streams lack well-defined channels and often split into multiple pathways. Occasionally, heavy rainfall along the Santa Cruz River southeast of the basin results in significant flows within the region[8].

According to the record of regional history, the agricultural activities have expanded since the late 1800s and have occupied almost all the alluvial surface in different periods. It is believed that one of the most important sources of water that was used to irrigate agriculture in the northern part of the basin was the removal of groundwater from the wells in the area. The basin also includes several towns that support the agricultural industry (Figure 2.1b). Florence and Coolidge are located near the Gila River in the northern part of the basin, while Eloy and Picacho are situated in the basin's center. Casa Grande, on the western boundary of the basin, is the largest community in the area, and this is also where the present thesis will continue to research in the later parts. The demand for water usage remained relatively small in the early ages, since only a limited number of indigenous people lived here before the arrivals of European settlers in the 1880s. These settlers began to build water supply systems for reclamation activities such as farming and building construction. The period from 1880s to 1920s is defined as the early development phase since little or no anthropogenic land subsidence or earth fissures were observed in this era. Significant consumption of water resources was seen after World War I as a result of the expansion of population and the increasing demand for agricultural products. From this period on, geohazards induced by human activities became more and more frequent.

(a) The domain of the Pichacho Basin and its surrounding area

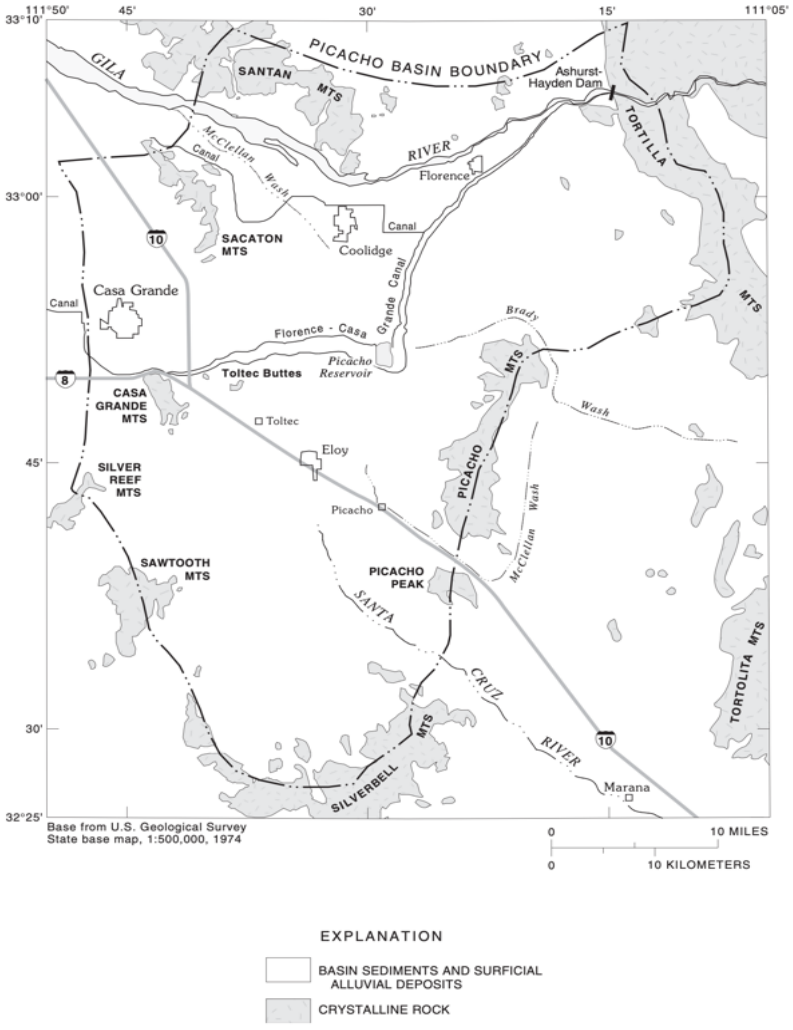

(b) Zoom in view of the Picacho Basin

Figure 2.1: Picacho Basin under different views

2.2 Climate Conditions in the Area

The study area is semi-arid, meaning little rainfall throughout the year. The average daily high temperature ranges from 19°C in January to 42°C in July, while the average daily low temperature ranges from 1°C in January to 24°C in July, with a yearly temperature of approximately 0°C to over 38°C[9].

At Coolidge, in the middle north of the Picacho Basin, annual precipitation averages about 210 mm. Rainfall may be slightly higher in the nearby mountains, but since the mountains only occupied a small portion of the entire basin and rise from 300 to 600 m high, the impact is limited. Precipitation records collected since 1931 in Casa Grande and Coolidge[9] show that the highest monthly rainfall is greater than 25 mm in July, August, and December; between 18 and 20 mm during most of the fall and winter months; and less than 8 mm from April through June. Long-term records at Coolidge have shown that annual precipitation varies by more than 127 mm. The extremes ranged from a high of 488 mm in 1941 to a low of 90 mm in 1956.

2.3 Geomorphology of the Study Area

Given the extensive size of the Picacho Basin, this study focuses on its western margin, where the Casa Grande mountain is located. This area was previously investigated by Jachens and Holzer (1982) [7], providing a well-documented record of land subsidence and earth fissures, along with proposed explanations for the observed phenomena. By selecting this specific region as the study area, we can leverage these comprehensive field observations to validate the effectiveness and advantages of the Peridynamics modeling framework. The application and demonstration of this system will be discussed in detail in subsequent chapters.

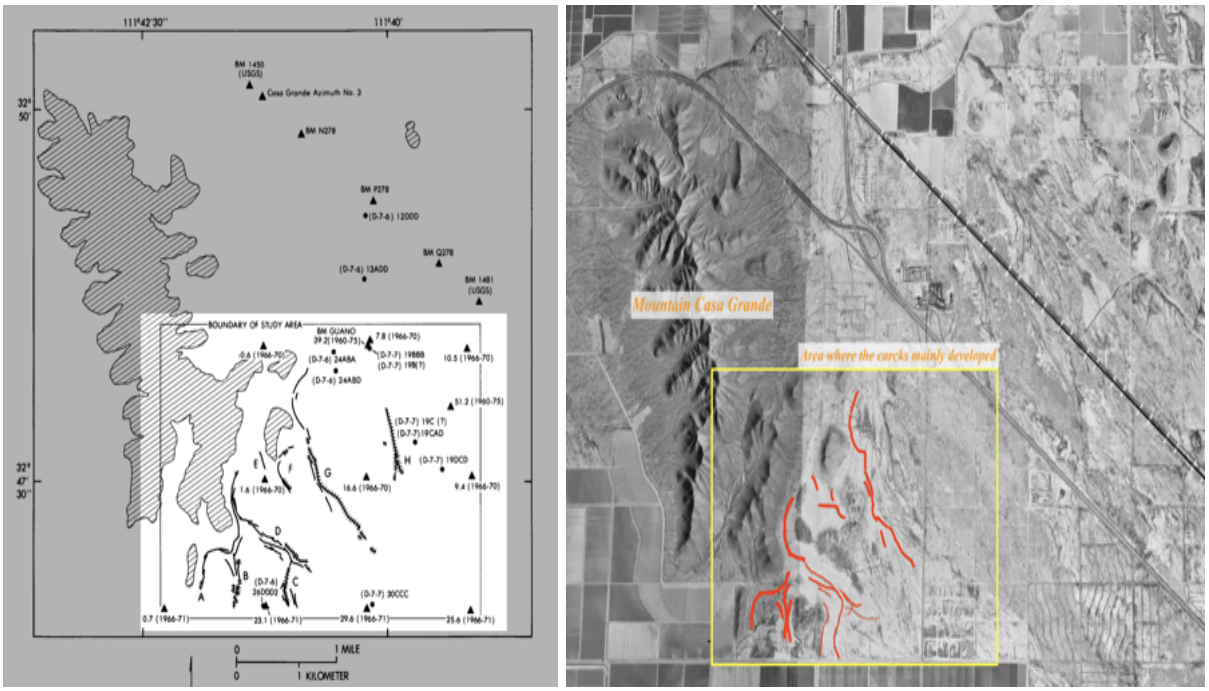

(a) Schematic diagram of the study area with benchmark locations and traces of the earth fissures

(b) Aerial photo of the study area with earth fissures indicated

Figure 2.2: The study area near Casa Grande Mountain

A further zoom-in view of the area around Casa Grande Mountain is provided in Figure 2.2, which shows a schematic diagram (Figure 2.2a) made by Holzer (1982) [7] and an aerial photo (Figure 2.2b) of the same place. Figure 2.2a shows the study area with traces of observed earth fissures and benchmark identifications with land subsidence data. It is worth noting that the numbers written in the lower labels

indicate the subsidence in centimeters and their recorded year. Meanwhile, Figure 2.2bprovides an aerial view of the region, where most of the cracks within the study area are emphasized with red curves.

The shallowest sediment layers underlying the study area are poorly sorted, but are believed to mainly consist of unconsolidated young alluvium, with crystalline rock or consolidated alluvium beneath. Although the exact thickness of these layers is not clearly defined, it is estimated that they exceed 700 m in depth near the central part of the study area.

2.4 Hydrogeologic Characterization

The available information on the hydrogeological features in the study area is mainly related to:

1. Records of the water levels and layer properties obtained from log of drilled wells.

   Four wells are available to characterize the hydro-stratigraphic setting. According to field investigations by Jachens and Holzer (1982) [7], in the northern boundary of the area, *Wells (D-7-7)19BBB and (D-7-6)24ABD* have penetrated unconsolidated coarse-grained until they reached the depth around $-75m$ below the surface, where clay unit begins noticeable. While *Wells (D-7-6)26DDD and (D-7-7)30CCC* located in the southern boundary, have penetrated unconsolidated coarse-grained layer until they reached the depth around $-100m$ below the surface, following by a clay layer as well. Wells in the northern and southern boundaries are $245m$ and $183m$ deep respectively, and both of them do not reach the clay layers. It is worthwhile to note that, a precise lithology underlying the unconsolidated alluvium in the study area remains unknown.

   Based on the hydrographs extracted from the area (Figure 2.3), water table changes were recorded in different wells whose locations are indicated in Figure 2.2a. Analysis of the composite hydrography shows that the water level was located $-18m$ below the land surface before 1940. It started to decline around the year of 1940, and stabilized at a depth of around $-58m$ in 1962, with a constant dropping rate from around 1940 to 1962. The total water table decline from 1940 to 1962 amounted to about $40m$.

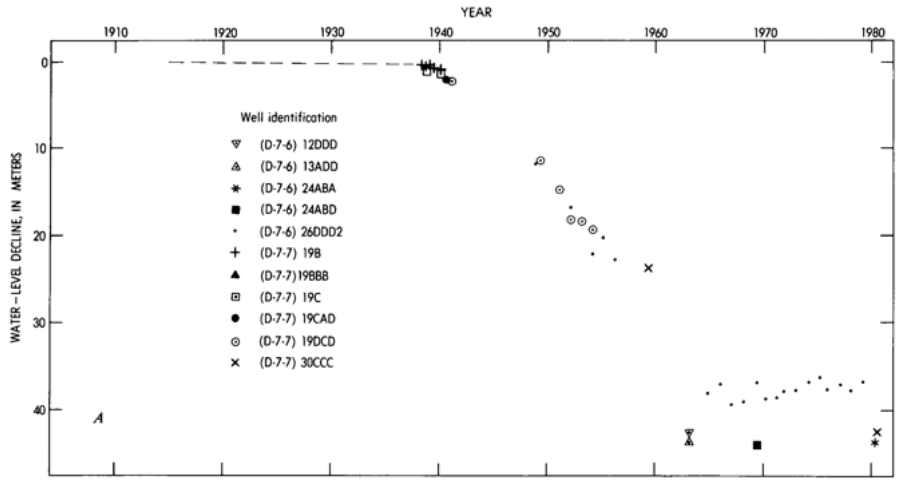

Figure 2.3: Composite hydrography based on 11 wells drilled in and near the basin

2. The topographic profiles of the bedrock obtained by the gravity measurement.

   From gravity measurements made at 369 locations within the study area by Jachens and Holzer (1982) [7], the topographic profiles of the buried bedrock were inferred by the analysis of Bouguer gravity field. A remarkable spatial correlation between many local gravity anomalies and the topographic profiles in the subsurface were found. A consistent pattern emerges across all of the more than 20 profiles examined: they exhibit a convex-upward shape at specific locations. This phenomenon is particularly evident at the crests of ridges in the gravity field and where abrupt changes

occur in the gravity field. It's noteworthy that this convex-upward characteristic is present in every profile, even in locations where the change in slope is subtle. This uniformity across numerous profiles suggests a significant correlation between the gravity field's features and the topographical characteristics of the profiles [7]. Figure 2.4 shows the results of the gravity measurements in terms of depth to bedrock beneath land surface, with hachures on contours pointing in direction of increasing depth.

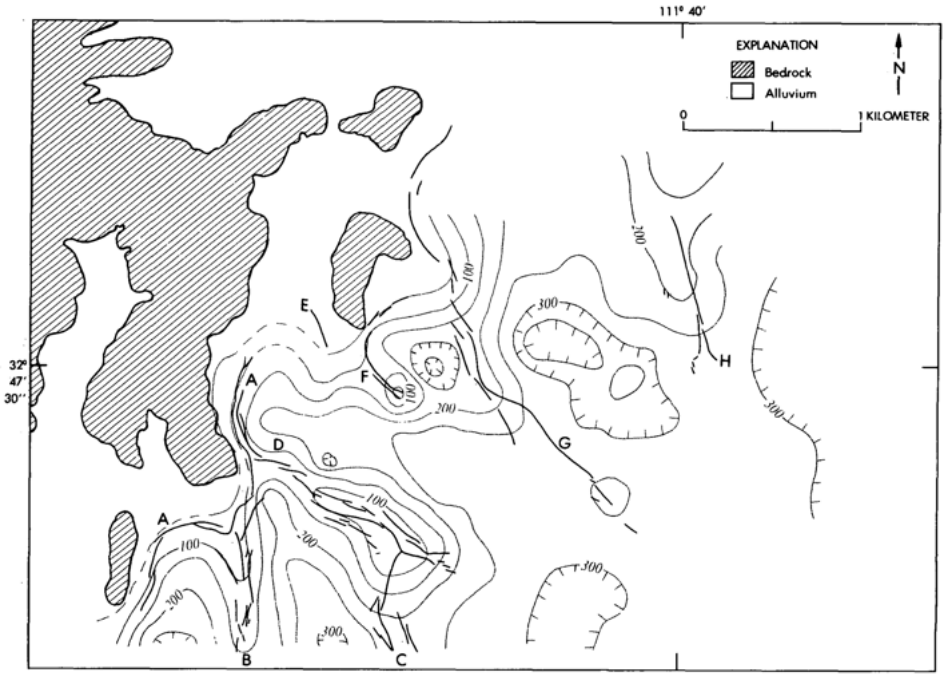

Figure 2.4: Map of inferred depth (m) to bedrock beneath land surface

2.5 Land Subsidence and Earth Fissures

Land subsidence and earth fissures observed in the area are largely attributed to human-induced factors, such as water level declines caused by agricultural activities. However, the immediate cause is the compaction of unconsolidated alluvium layers.

Land subsidence

Approximately 1200 km^2 of the basin experienced land subsidence of 0.3 m or more between 1934 and 1977, with a maximum subsidence of 3.8 m occurring in the east-central part of the basin. As the water level began to decline around 1940, basin subsidence is presumed to have commenced after 1948. Unlike the relatively steady rate of water level decline, subsidence rates were variable during the investigation period but began to decrease in the early 1960s. Jachens and Holzer (1982) [7] summarized the history of land subsidence at six reference locations north of the study area, reporting subsidence ranging from 0.39 m to approximately 0.81 m between 1960 and 1975 (Figure 2.5). A normalization analysis of these subsidence curves revealed that 49% of the total subsidence occurred during this period. The locations corresponding to these curves are shown in Figure 2.2.

To further examine the southwest corner of the study area, where fissure zones A, B, and C are located, a localized view is provided in Figure 2.6. From the well *(D-7-6) 26DDD2* records, the land subsidence between fissure zones B and C was documented in 23.1 cm until 1966. The total subsidence at this well was estimated in 47.1 cm until 1980 [7].

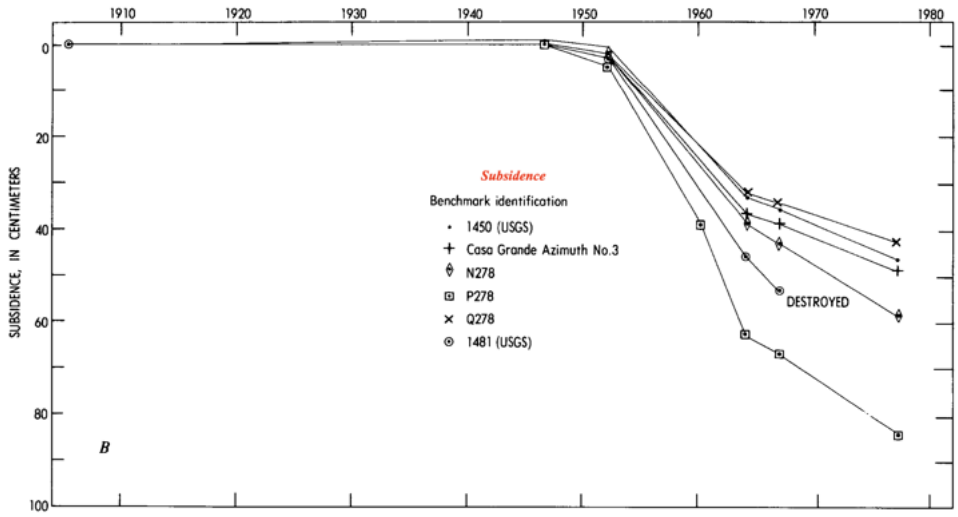

Figure 2.5: Land subsidence history at the six benchmarks whose locations are shown in Figure 2.2.

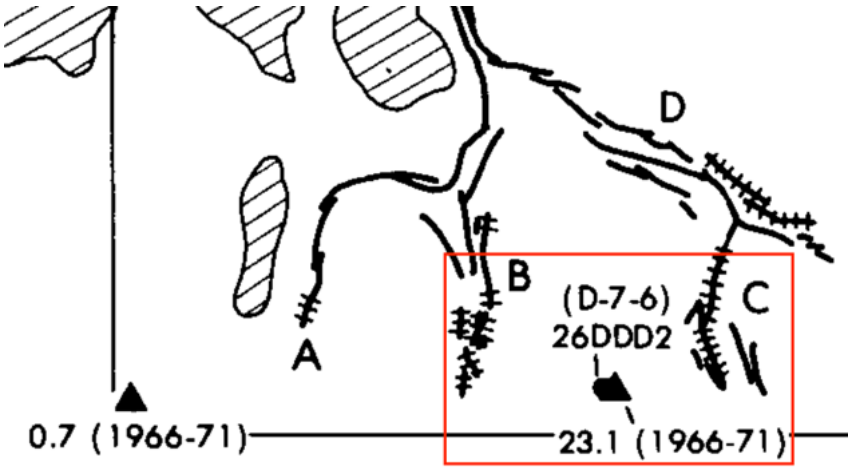

Figure 2.6: Land subsidence at southwest corner of the study area

Earth fissures

As shown in Figure 2.2, earth fissures are widely distributed within the study area, with considerable variation in their cross-sectional forms and dimensions. According to field investigations by Jachens and Holzer (1982) [7], these differences in shape and size are primarily attributed to modifications caused by erosion, deposition, and the amount of tensile strain relieved by each fissure. During the study period, the average fissure width was approximately 3 m, with depths exceeding 4 m. Observations also revealed variability in the horizontal movements that contributed to the formation of these fissures.

Some fissure zones have become inactive and their fissures were fully or partially filled by sediments. However, Zone C highlighted in Figure 2.2 remained active, as confirmed by aerial photographs analysis.

Chapter 3

Mechanisms and Methodology

3.1 Geomechanical Explanation on Land Subsidence

The phenomenon of land subsidence can result from natural processes or anthropogenic activities; however, the underlying mechanisms are often similar. To provide a comprehensive explanation of the mechanisms driving land subsidence, it is essential to first introduce several key concepts.

3.1.1 Effective Stress

It is widely recognized that one of the most significant factors contributing to land subsidence is the increase in effective stress. In the early 1920s, Karl Terzaghi introduced the theory of effective stress to describe stress relationships within a three-phase soil element (comprising solids, water, and air). This theory has become fundamental to understanding soil behavior under load. Terzaghi's formulation is based on the following assumptions:

1. The solid particles are in contact and the particles are incompressible.
2. The degree of soil saturation is equal to 1 (i.e. the volume is composed of two phases: solids and water)
3. Strains in the soil are small.

When the above assumptions are satisfied, the total compressive stress applied normal to a particular plane, σ_{total}, is defined as the sum of the effective compressive stress, σ', and the pore water pressure, u_w. This relationship can be mathematically expressed as follows:

$$\sigma_{total} = \sigma' + u_w \tag{3.1}$$

Equation 3.1 illustrates this fundamental principle of Terzaghi's effective stress theory.

As Terzaghi's theory is fundamental to soil mechanics analysis, it is crucial to adhere to the same assumptions when constructing the numerical model to ensure the theory applicability. Consequently, the unit weight of saturated soil, γ_s, that is the unit weight of the bulk, γ_b, is assumed to remain constant throughout the simulation when a confined aquifer is considered. This assumption implies that the total stress, $\sigma_{total} = \gamma_b z$, remains constant at any depth z within the subsiding soil layers.

As a result, to satisfy the effective stress equation $\sigma_{total} = \sigma' + u_w$, the effective stress σ' must increase when the pore water pressure, u_w, decreases due to a decline in the water table. This ensures that the relationship defined by Equation 3.1 is valid during the simulation.

It is important to note that the relationship between total stress, effective stress, and pore water pressure remains valid in the modeling system, whether using the Peridynamics theory or the Finite Element Method, provided that the underlying assumptions are upheld. Consequently, changes in effective

stress will be treated as the primary cause of land subsidence and earth fissures in our Peridynamics model. A detailed explanation of this approach will be provided in the subsequent chapters.

3.1.2 Terzaghi's Consolidation Theory

Within the domain of classical continuum theory, which is the most widely utilized nowadays, a relation founded by Terzaghi between the increase in effective pressure and the reduction of void ratio reads [10]:

$$e_u = e_i - C_c \ln \frac{\sigma' + \Delta\sigma'}{\sigma'} \tag{3.2}$$

where e denotes the void ratio, and

e_u = ultimate void ratio

e_i = initial void ratio

C_c = compressive index

σ' = initial effective pressure of the soil layer before the lowering of water table

$\Delta\sigma'$ = Increase in effective stress after the lowering of water table

In a saturated configuration, the soil volume V_t is composed only of the solid volume V_s and the water volume V_w. Since the solids are incompressible and V_s remains unchanged, the subsidence can be solely attributed to the loss of void volume:

$$\eta = s_0 \frac{e_i - e_u}{1 + e_i} \tag{3.3}$$

where η is the layer compaction and s_0 is the original thickness of the layer.

By substituting Equation 3.2 in Equation 3.3, we can obtain the relation between the subsidence and the increment of effective pressure:

$$\eta = s_0 \frac{1 + e_i}{C_c} \ln \frac{\sigma' + \Delta\sigma'}{\sigma'} \tag{3.4}$$

Let $c = C_c/(1 + e_i)$ the compression constant, Equation 3.4 can be further simplified as:

$$\eta = s_0 \frac{1}{c} \ln \frac{\sigma' + \Delta\sigma'}{\sigma'} \tag{3.5}$$

The value of the compression constant depends on the type of soil; if this constant is known, land subsidence can be calculated. However, it is usually difficult to determine the exact value of c for a specific soil. Table 3.1 provides the ranges of values for various types of soils.

Soil Type	**Range of compression constant c**
Sand, densely packed	100 - 200
Sand, loosely packed	20 - 100
Clay loam	20 - 30
Clay	10 -25
Peat	2 - 10

Table 3.1: Range of compression constant for different types.

3.2 Geomechanical Explanation on Earth Fissures

The formation of earth fissures has been extensively studied in the context of both natural events and human activities. The relationship between earth fissures and land subsidence is complex and nuanced. Some researchers have proposed that differential subsidence, which causes bending of the Earth's surface,

is the primary mechanism behind the formation of earth fissures [7][11][12]. Others have suggested that earth fissures are the result of horizontal movements within aquifers caused by changes in the water table in unconsolidated aquifer systems [13][14]. In the Picacho Basin, it was suggested that fissuring was produced by lowering groundwater levels or the associated land subsidence [15].

Coulomb-Mohr's Criterion

Consider an aquifer system as depicted in Figure 3.1, where Point A and Point B represent two distinct locations indicated by arrows in the diagram. Although the distance between these points is relatively small, it is sufficient to capture the variations in vertical stresses. To better illustrate the mechanics of fissuring, which can be explained using Coulomb-Mohr's criterion, we zoom in and extract a soil element from the system. In this element, point B corresponds to the upper left corner, while point A represents the upper right corner (Figure 3.2).

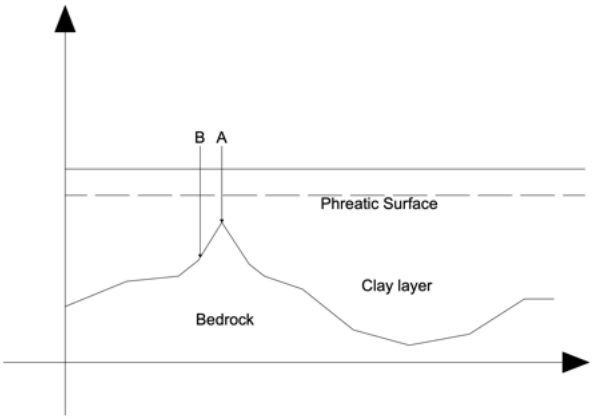

Figure 3.1: Typical aquifer system comprised by clay and bedrock.

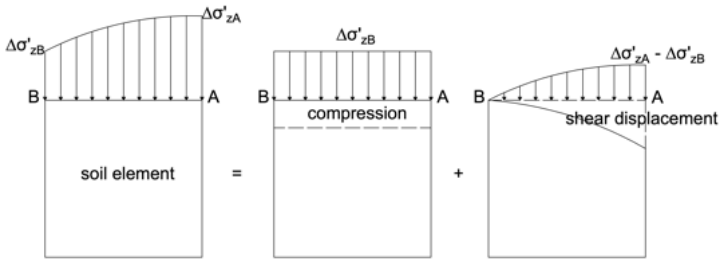

Figure 3.2: The change of effective stress in a soil element.

As shown in the figure, the soil element is located at a depth below the phreatic surface within an unconfined aquifer. When the groundwater level declines, the pore pressure of the sediments decreases. According to Equation 3.1, this reduction in pore pressure leads to an increase in effective stresses along the straight line connecting Points A and B, provided that the total stresses (e.g. external loads) remain unchanged.

The decline in groundwater level is generally not uniform along a horizontal line between A and B. In such cases, the changes in effective stress from A to B are not identical, leading to the development of shear displacements. This scenario is depicted in Figure 3.2, where $\Delta\sigma'_{zB}$ and $\Delta\sigma'_{zA}$ represent the distinct changes in effective stress at Points B and A, respectively [16].

According to Mohr-Coulomb Failure criterion, the limit shear strength a soil is able to experience without fissuring is ruled by the following equation (Figure 3.3):

$$\tau_L = c - \sigma' \tan\phi \tag{3.6}$$

where c is the cohesion of the soil, ϕ is the internal friction angle of the soil, and σ' is the vertical effective stress. The shear strength can be determined by different types of tests such as the *Direct Shear Test* and the *Triaxial Test*.

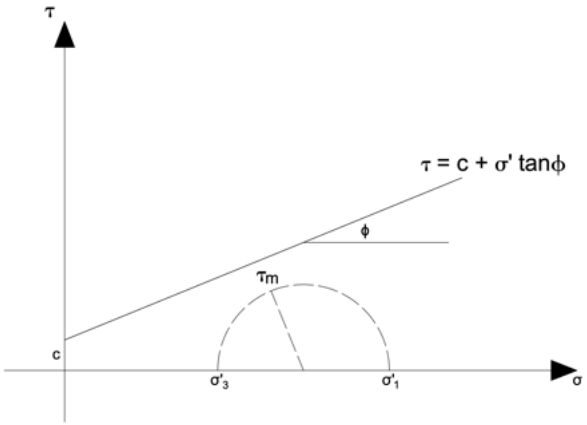

Figure 3.3: Relationship between shear strength and effective stress

If the maximum shear stress τ_m defined by the maximum effective stress difference $\Delta\sigma'_{zB} - \Delta\sigma'_{zA}$ lies above the curve $\tau_L = c - \sigma' \tan\phi$, it means that the soil is loaded to failure due to the excessive shear stress and therefore cracks form.

3.3 Peridynamics modeling framework

To simulate land subsidence and earth fissures in a numerical model, it is essential to incorporate mathematical expressions that describe the relationship between stress changes, displacement, time, and space. In classical continuum theory, the Finite Element Method (FEM) is commonly employed to calculate land subsidence. By solving partial differential equations (PDEs) that describe the motion of nodes within a mesh over time and space, land subsidence can be determined.

Starting from Terzaghi (1923) [10] theory, Biot (1941) [17] generalized the equilibrium equations to three-dimensional (3D) porous media. Accordingly, the following poroelastic model is applied to describe the consolidation of aquifer systems:

$$K\left(\frac{\partial^2 p}{\partial x^2} + \frac{\partial^2 p}{\partial y^2} + \frac{\partial^2 p}{\partial z^2}\right) = \phi\beta\frac{\partial p}{\partial t} + \frac{\partial \epsilon}{\partial t} + f \tag{3.7}$$

$$\mu\nabla^2\mathbf{u} + (\lambda + \mu)\nabla(\nabla \cdot \mathbf{u}) = \nabla p \tag{3.8}$$

where,

- K is the hydraulic conductivity of the porous medium;
- ϕ is the porosity;
- β is the compressibility of fluid, measuring how fluid volume change under pressure;
- f is the external source or sink term (e.g., injection or extraction of fluid);
- $\left(\frac{\partial^2 p}{\partial x^2} + \frac{\partial^2 p}{\partial y^2} + \frac{\partial^2 p}{\partial z^2}\right)$ represents the Laplacian operator of pressure head, describing the variation of fluid pressure in the three-dimensional space;
- $\frac{\partial p}{\partial t}$ represents the fluid pressure change over time, indicating the evolution of fluid diffusion within the system over time;
- $\frac{\partial \epsilon}{\partial t}$ represents volumetric strain of the porous medium over time;
- $\mathbf{u}$ is the displacement vector field;
- μ is the shear modulus, representing the material's resistance to shear deformation;
- λ is the first Lame parameter, related to the material's resistance to volumetric deformation.

It is worth noting that, the relationship between displacement vector field $\mathbf{u}$ and volumetric strain ϵ can be expressed by the following equation:

$$\epsilon = \frac{1}{2}\left(\nabla\mathbf{u} + (\nabla\mathbf{u})^T\right) \tag{3.9}$$

Equation 3.7 described the groundwater flow, while Equations 3.8 describe the equilibrium of the 3D porous system experiencing a certain pressure change and, consequently, allow computing the 3D displacement field. The classical integration of equations 3.7 and 3.8 by FEM is based on the assumption that the mesh nodes only interact with their immediate vicinity. As a result, whenever an earth fissure develops, the equations will immediately breakdown since the displacement field becomes discontinuous. In other words, in the classical continuous approach solved by FEM, the simulation of crack development is challenging.

In order to overcome this problem, a continuum theory that employs a non-local model named *Peridynamics* was proposed by Silling (2000) [6]. Peridynamics does not distinguish between points in a body where a discontinuity in displacement or its spatial derivatives may be located [6]. The particles in a Peridynamics model are assumed to be separated by a finite distance and to be able to interact with each other. Rather than describing the particles motion by using the partial differential equations, the fundamental difference in Peridynamics model is that it uses spatial integral formulation. The Peridynamics constitutive model is different from the traditional local constitutive models as it does not contain the displacement gradient. Therefore, it is still valid in the presence of any displacement discontinuity.

With these inherent characteristics, Peridynamics is particularly suitable for the simulation of cracks in geomaterials. The Peridynamics theory includes three different types: bond-based Peridynamics, ordinary state-based Peridynamics, and non-ordinary state-based Peridynamics. In the present paper, the simulator developed by Ye et al. (2024) [4] and implementing an *ordinary state-based Peridynamics* is used. The equation of motion can be described by the following [5]:

$$\rho(\mathbf{x})\ddot{\mathbf{u}}(\mathbf{x},t) = \int_{\mathcal{H}_\mathbf{x}} \{\underline{\mathrm{T}}\,[\mathbf{x},t]\,\langle \mathbf{x}\prime - \mathbf{x}\rangle - \underline{\mathrm{T}}\,[\mathbf{x}\prime,t]\,\langle \mathbf{x} - \mathbf{x}\prime\rangle\} dV_{\mathbf{x}\prime} + \mathbf{b}(\mathbf{x},t) \tag{3.10}$$

where
$\mathcal{H}_\mathbf{x}$ called *Horizon* is a spherical neighborhood of radius δ centered at particle point $\mathbf{x}$;
$V_{\mathbf{x}'}$ is the volume of particle $\mathbf{x}'$
$\mathbf{u}$ is the displacement vector field;
ρ is the mass density of point $\mathbf{x}$;
$\mathbf{b}$ is the *body force density field*.
$\underline{\mathrm{T}}$ is the *force vector state field*, it is an infinite-dimensional array that stores all of the force density vectors, $\mathbf{t}_{(k)(j)}$ with $(j = 1, 2, ..., \infty)$;

In general, the term *force vector state field* $\underline{\mathrm{T}}$ can be expressed mathematically by the following equation:

$$\underline{\mathrm{T}}(\mathbf{x}_{(k)},t) = \begin{Bmatrix} \mathbf{t}_{(k)(1)} \\ \vdots \\ \mathbf{t}_{(k)(\infty)} \end{Bmatrix} \tag{3.11}$$

It is assumed that:

- $\underline{\mathrm{T}}$ is Riemann integrable and that the integral in Equation 3.10 converges uniformly;
- $\underline{\mathrm{T}}$ satisfies the balance of linear momentum for any bounded body $\mathcal{B}$, so that

$$\int_\mathcal{B} \rho\ddot{\mathbf{u}}(\mathbf{x},t)dV_\mathbf{x} = \int_\mathcal{B} \mathbf{b}(\mathbf{x},t)dV_\mathbf{x} \qquad \forall t \leq 0 \tag{3.12}$$

It is worth noting that, in the case of land subsidence and earth fissures modeling, the movement of the particles can be considered as quasi-static. Thus, the terms $\ddot{\mathbf{u}}(\mathbf{x},t)$ in Equation 3.10 is set equal to 0.

The term $\xi = \mathbf{x}' - \mathbf{x}$ represents the relative position of two material points (the bond) in the reference configuration. The relative displacement between point x and point x' can be denoted by $\eta = \mathbf{u}' - \mathbf{u}$. Defining through $\mathbf{y}$ and $\mathbf{y}'$ the same particle points $\mathbf{x}$ and $\mathbf{x}'$ in the deformation state, it can be written $\underline{\mathrm{Y}}\langle \mathbf{x}' - \mathbf{x}\rangle = \mathbf{y}' - \mathbf{y} = \xi + \eta$.

To further construct the constitutive model under the Peridynamics framework, it is necessary to introduce the concept of *peridynamcis constitutive correspondence* [5]. The fundamental idea is that the

changes strain energy in both classical and Peridynamics theories must be equal under affine deformations (i.e., homogeneous deformations). Thus, we need to cast a traditional constitutive model into the state-based Peridynamics framework and determine an approximation to the local deformation gradient, F, for each material point:

$$K = \int_{\mathcal{H}_{\mathbf{x}}} \omega(\|\xi\|)(\xi \otimes \xi) dV_{\mathbf{x}'} \tag{3.13}$$

$$F = \left[\int_{\mathcal{H}_{\mathbf{x}}} \omega(\|\xi\|)(\underline{Y} \otimes \xi) dV_{\mathbf{x}'}\right] K^{-1} \tag{3.14}$$

where,
K is the so-called Shape Tensor, which is positive-definite and always invertible;
F is the approximate deformation gradient at material point x;
ω is the *influence function*, it qualifies the relative influence of one material point on another within its *Horizon*, defining how interactions are weighted between points in the material;
The symbol $\otimes$ represents the dyadic product of two vectors.

Then according to Green-Lagrange Strain, the relation between strain and deformation gradient is as follow:

$$\epsilon = \frac{1}{2}(F^T \cdot F - I) \tag{3.15}$$

where, ϵ is the volumetric strain and I is a 6×6 identity matrix.

As in the current context the deformation of the soil is assumed to be linear isotropic elastic, the effective stress tensor σ' can be calculated by the stiffness matrix and the strain of the soil:

$$\sigma' = D \cdot \epsilon \tag{3.16}$$

where, D is the *stiffness matrix* and

$$D = \frac{E(1-\nu)}{(1+\nu)(1-2\nu)} \begin{bmatrix} 1 & \frac{\nu}{(1-\nu)} & \frac{\nu}{(1-\nu)} & 0 & 0 & 0 \\ \frac{\nu}{(1-\nu)} & 1 & \frac{\nu}{(1-\nu)} & 0 & 0 & 0 \\ \frac{\nu}{(1-\nu)} & \frac{\nu}{(1-\nu)} & 1 & 0 & 0 & 0 \\ 0 & 0 & 0 & \frac{1-2\nu}{2(1-\nu)} & 0 & 0 \\ 0 & 0 & 0 & 0 & \frac{1-2\nu}{2(1-\nu)} & 0 \\ 0 & 0 & 0 & 0 & 0 & \frac{1-2\nu}{2(1-\nu)} \end{bmatrix} \tag{3.17}$$

To make the strain-stress relationship more straightforward, Equation 3.16 can be rewritten as follow:

$$\begin{bmatrix} \sigma'_{xx} \\ \sigma'_{yy} \\ \sigma'_{zz} \\ \sigma'_{yz} \\ \sigma'_{xz} \\ \sigma'_{xy} \end{bmatrix} = \frac{E(1-\nu)}{(1+\nu)(1-2\nu)} \begin{bmatrix} 1 & \frac{\nu}{(1-\nu)} & \frac{\nu}{(1-\nu)} & 0 & 0 & 0 \\ \frac{\nu}{(1-\nu)} & 1 & \frac{\nu}{(1-\nu)} & 0 & 0 & 0 \\ \frac{\nu}{(1-\nu)} & \frac{\nu}{(1-\nu)} & 1 & 0 & 0 & 0 \\ 0 & 0 & 0 & \frac{1-2\nu}{2(1-\nu)} & 0 & 0 \\ 0 & 0 & 0 & 0 & \frac{1-2\nu}{2(1-\nu)} & 0 \\ 0 & 0 & 0 & 0 & 0 & \frac{1-2\nu}{2(1-\nu)} \end{bmatrix} \cdot \begin{bmatrix} \epsilon_{xx} \\ \epsilon_{yy} \\ \epsilon_{zz} \\ 2\epsilon_{yz} \\ 2\epsilon_{xz} \\ 2\epsilon_{xy} \end{bmatrix} \tag{3.18}$$

According to Ye et al. (2024) [4], the damage Ψ to a PD material point $\mathbf{x}$ can be given locally in terms of the ratio between the number of broken bonds with respect to the total amount of interaction on the horizon [6]:

$$\Psi(\mathbf{x}, t) = 1 - \frac{\int_{\mathcal{H}_{\mathbf{x}}} \mu(t, \boldsymbol{\xi}) \, \mathrm{d}V_{\boldsymbol{\xi}}}{\int_{\mathcal{H}_{\mathbf{x}}} \mathrm{d}V_{\boldsymbol{\xi}}}, \tag{3.19}$$

where $\mu(t, \boldsymbol{\xi})$ is a scalar factor representing the conditional breakage of a bond:

$$\mu(t, \boldsymbol{\xi}) = \begin{cases} 1 & \text{if } \|\boldsymbol{\tau}\| \leq \tau \text{ or } S_N \geq 0, \\ 0 & \text{otherwise.} \end{cases} \tag{3.20}$$

Fissure is expected to develop if at least 50% of the bonds around a material point break, i.e. $\Psi > 0.5$.

Chapter 4

Numerical Model Set-up And Testing

4.1 Peridynamics Simulator in Python

For the Peridynamics modeling framework adopted in the present thesis, refer to Ye et al. (2024) [4]. The performance of this Python-implemented code has been proven in various applications of land subsidence and earth fissure simulation in case studies in China. In order to further investigate the applicability of this newly established modeling framework on a wider arrange of aquifers and aquitards with different settings in many other places, we applied this Peridynamics simulator to compute land subsidence and earth fissures in Picacho Basin, Arizona.

According to the present PD modeling framework, isotropic linear elastic materials have been assumed.

To favor its applicability, the simulator is divided into two parts, which are the *parameters* part and the *PD model* part. While the content of the former part need to be changed according to different case studies, the latter part remain largely unchanged.

The Parameters part

The part of *Parameters* is used to describe the numerous parameters of the model, including (not exclusively):

- the size of the model such as length, width and depth;
- the distance of two particle points, and the horizon of each material point;
- the distribution of subsurface layers and their hydro-geomechanical properties;
- the evolution of the water table and its applied domain;
- the initial boundary conditions;
- the number of time steps.

However, these parameters must be determined on a case-by-case basis. For example, in the case study of the Picacho Basin, the scale of the simulation domain is relatively large, necessitating a point-to-point distance of 5 m to reduce the computational expense. In addition, to ensure that the simulation process is fully completed, the maximum number of time steps is determined using a trial-and-error approach. As these parameters serve as initial input to the model, they exert a decisive influence on the accuracy of the results. Therefore, careful consideration is required for each case study to achieve reliable and precise outcomes.

The PD Model part

The *PD Model* component contains the core algorithm to simulate land subsidence and earth fissures. It takes input from the parameters section and, based on the explicitly prescribed constitutive relationships within the system, calculates the motion of particles. The model iterates until it reaches the maximum number of time steps, which is manually set beforehand. At the end of each time step, key information, such as updated particle coordinates, is stored and then used as input for subsequent time steps. Once the entire stepping process is completed, the final results are obtained for land subsidence and earth fissure development.

4.2 Set-up of a Simplified Test Case

Since the simulator based on Peridynamics theory represents, to some extent, a novel approach, it is essential to construct two identical simple models to examine the differences between the new modeling framework and the classical continuum modeling framework. These models are designed to have the same dimensions, layer configurations, soil properties, and water table decline.

In one model, the domain is represented by discrete meshless material points, which is used for the Peridynamics-based simulation. The other model is constructed using a refined mesh network that includes both standard nodes and elements, as well as interface elements, and is employed in the simulation based on the Finite Element with Interface Elements (FE-IE). The primary objective is to compare the results obtained from the Peridynamics simulation with those produced by the FE-IE simulator on the same case tests. Given that the traditional FE-IE approach has been extensively validated and is considered highly reliable [18] [19] [20], a minimal discrepancy between the results of the two methods would serve as strong evidence for the feasibility and reliability of the Peridynamics approach.

The classical continuum theory has been extensively developed and is widely accepted within the industry for land subsidence simulations. However, since earth fissures cannot be directly computed in the continuum framework, they can be addressed by incorporating special **interface elements** into the FE mesh. However, this approach requires prior knowledge of the crack positions, which can be challenging to determine in many cases. In contrast, the Peridynamics modeling framework allows for spontaneous simulation of earth fissure development without the need to predefine fissure locations or interfere within the model. If the accuracy of the results obtained from Peridynamics can be validated, it has the potential to revolutionize the simulation of earth fissures by removing the constraints imposed by traditional methods.

Simple Model in Peridynamics

The configuration of the simple model to be used in Peridynamics is shown in Figure 4.1.

The model dimensions are 500 m in length, 300 m in height, and 35 m in width, with a material point spacing equal to 5 m. The red domain in the figure represents a rock ridge, while the blue material points correspond to the unconsolidated alluvium layer. To ensure the physical validity of the soil properties, the model adopts parameters derived from the Picacho Basin case study. For example, the densities of the unconsolidated alluvium layer and base rock layer are set to 2.1 g/cm^3 and 2.6 g/cm^3, respectively. Concerning Young's modulus (E) and Poisson's ratio (ν), empirical values are employed for these parameters, i.e. $E = 1.5 \times 10^8$ Pa and $\nu = 0.25$.

In addition, it is necessary to define the water table decline, as it serves as the primary driver of land subsidence and subsequent earth fissures. A total water table decline of 40 m is applied, matching the conditions used in the Picacho Basin model described in later sections. Specifically, the initial water table is set at 18 m below the land surface, while the final water table is positioned at 58 m below the land surface. To effectively simulate this process, the number of time steps is set to a sufficiently large value (i.e. 500) to allow the simulator to reproduce properly the motion of the material points. During these time steps, the pore water pressure in the model decreases proportionally to the computational steps, ensuring a gradual and realistic simulation of water table decline.

Boundary conditions are also crucial in this model. For particles located along the left and right edges of the model, their displacements along the Y-axis are precluded. Similarly, particles located

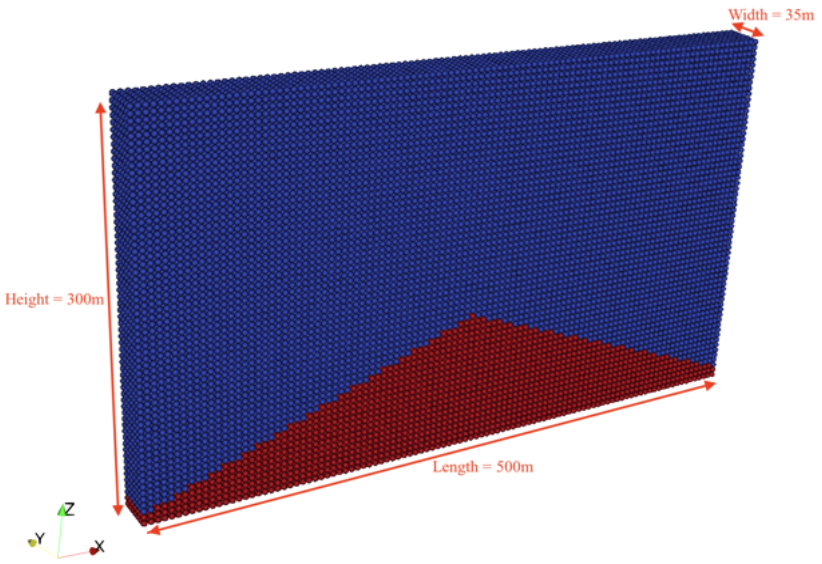

Figure 4.1: Simple Model in Peridynamics

along the front and back edges have displacements precluded along the X-axis. In addition, material points along the bottom are fully constrained, preventing movement in all directions. In the context of Peridynamics, the term "edge" is extended beyond the material points on the boundary of the model to include a region as deep as twice the point-to-point distance from the physical edge.

In summary, we have established conditions in which all parameters, except the profile of the underlying bedrock, are identical to those used in the Picacho Basin case study.

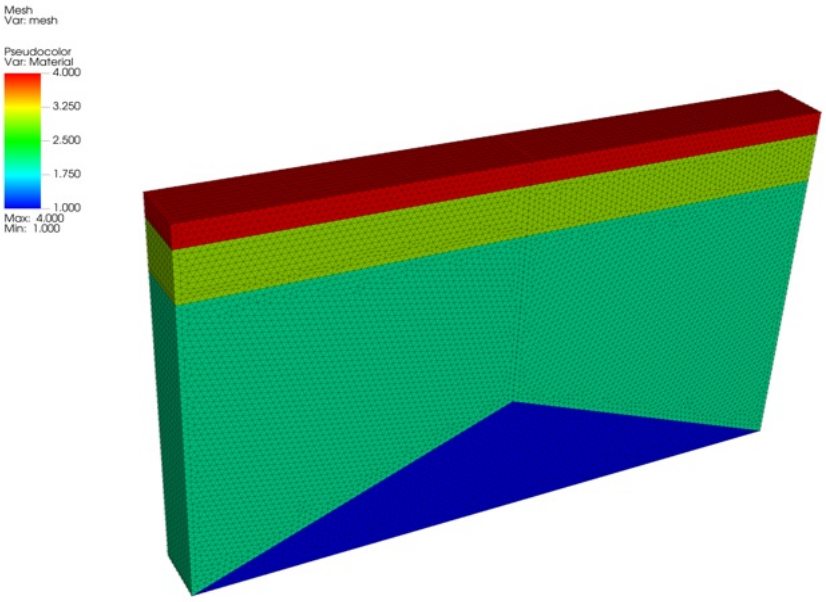

Figure 4.2: The mesh developed to discretize the simple model with layers indicated

Simple Model in FE-IE

GEPS3D is the Finite Element simulator used in the current thesis. GEPS3D is based on classical continuum theory and was developed by the Department of Civil, Environmental and Architectural Engineering, University of Padova. The mesh used to discretize the simple model can be seen in Figure 4.2

Unlike the "two-layer" structure in the Peridynamics model, the continuum model incorporates four layers to better capture the changes in pore water pressure within the mesh. The top three layers are composed of the same material, i.e., unconsolidated alluvium, with identical properties. The bottom layer, indicated by the red triangle in the figure, represents the bedrock ridge and is identical in terms of shape and size to the one used in the Peridynamics model. The model starts with an 18 m thick top layer, represented by the dark blue color in the figure. Below this, the second layer is 40 m thick, followed by the third layer beneath it. For clarity, the layers are numbered from top to bottom as layers 1 through 4. Layers 1 through 3 are assigned a density of 2.1 g/cm^3, while layer 4 (the bedrock) is assigned a density of 2.6 g/cm^3.

Another key difference between the FE-IE model and the PD model lies in the need to pre-define crack positions in the FE framework. In GEPS3D, for example, the position of any fissure expected to develop must be specified beforehand. To illustrate, consider the simple case model. For simplicity, only one crack is anticipated to develop and its location is assumed to extend from the top center of the model to the tip of the bedrock layer. By specifying the nodes along the path where the fissure is expected, a 2D plane composed of interface elements is created and inserted into the 3D FE mesh, as shown in Figure 4.3.

It is worth noting that in the GEPS3D model, compressibilities must be defined for each soil layer instead of Young's modulus, as used in the Peridynamics model. Using the explicit relationship between the Poisson ratio ν, Young's modulus E, and compressibility c_m (Equation 4.1), the compressibility values corresponding to Young's modulus applied in the Peridynamics model can be calculated and assigned accordingly.

$$c_m = \frac{(1+\nu)(1-2\nu)}{E(1-\nu)} \tag{4.1}$$

Given that we employed $\nu = 0.25$ and $E = 1.5 \times 10^8$ Pa in the Peridynamics model, the corresponding compressiblity for the GEPS3D model is calculated as $c_m = 5.55 \times 10^{-9}$ Pa^{-1}.

In addition, boundary and initial conditions must be assigned:

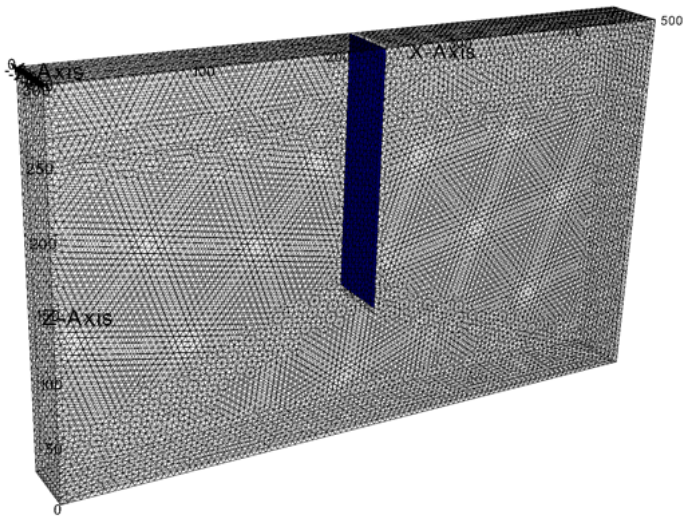

Figure 4.3: The Interface Element inserted in the original mesh

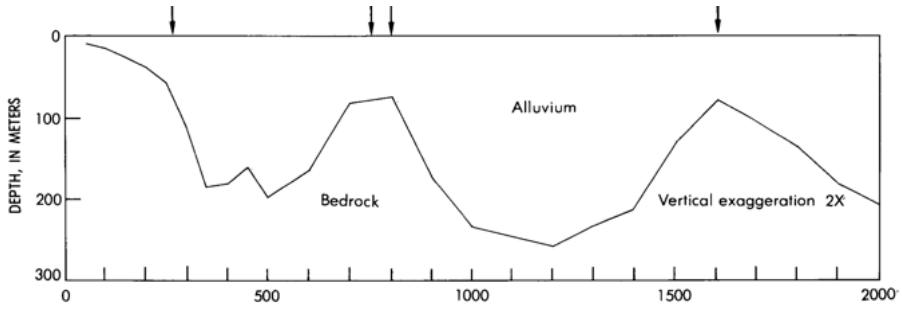

Figure 4.4: Surface topography in April 1980 and inferred configuration of buried bedrock surface along the profiles in the study area. The arrows added on the land surface represent indicate the locations of the fissures. The vertical depth of the profile has been exaggerated by a factor of 2 relative to its horizontal length for clarity.

- Boundary Conditions: the nodes on the model boundaries except the top boundary must be identified. The displacements of these nodes are precluded at every time step to reflect the structural boundary conditions of the model.
- Pressure Changes: to ensure a proper comparison with the Peridynamics outcomes, the same pressure changes observed in the hydrographic data from the Picacho Basin are applied to the model.

4.3 The Picacho Model Set-up

As it stated in Section 2.2, the surface topography in April 1980 and the inferred configuration of the buried bedrock surface along the profiles in the study area are shown in Figure 4.4,

The selected profile consists of a two-layer structure with unconsolidated alluvium overlying a bedrock layer. Notice the arrows at the top of the figure that indicate the locations of the fissures as observed in the field. The shape of the bedrock profile was inferred from Bouguer gravity measurements.

4.3.1 From Land Profile to the Model

Before performing the simulation, the model must be initialized. The initialization process involves several steps, the first being the determination of the size of the model and the distance between particles. This allows the simulator to generate the model domain suitable for defining various parameters in

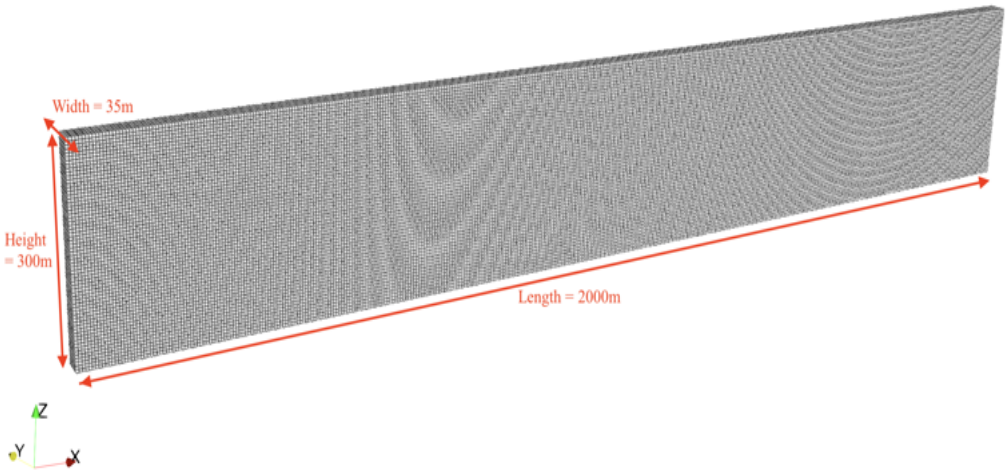

Figure 4.5: The array of material points forming the model domain.

subsequent steps. In the present case, the size of the model domain is set to 2000 m in length $\times$ 300 m in height $\times$ 35 m in width. The choice of point-to-point distance considers two main factors:

- Computational Feasibility: the distance should not be too small to avoid excessive computational expense, ensuring the simulation remains manageable for the available hardware.
- Model Resolution: the distance should not be too large to ensure that critical developments, such as each fissure formation, can be accurately represented in the model.

To balance these concerns, the point-to-point distance in the current model is set to 5 m. Figure 4.5 shows the model domain, where the size and point-to-point distance are defined by means of a simple code.

At this stage, the model is merely a cube composed of numerous points without any physical significance. To further develop the model, the next step involves incorporating the bedrock profile derived from field investigations into the Peridynamics modeling framework. This requires representing the bedrock profile to clearly delineate the interface between the two different materials. To achieve this goal, a polynomial function is used to approximate the bedrock profile. However, the extracted profile from the study area is highly irregular and contains numerous inflection points that are nondifferentiable. Since any continuous curve represented by a polynomial must be differentiable, the original bedrock profile must be smoothed. To ensure that the artificial curve remains as close as possible to the original profile, a polynomial of degree 10 is adopted.

The process of "digitizing" the profile curve can be broadly divided into two steps:

1. Redraw the curve by AUTO-CAD. According to the length and depth of the profile given in Figure 4.4, we recreate a curve that follows the real scale of 1:1 in vertical to horizontal. The main idea is to capture a number of key coordinate information originated from the profile so that these data can be used as the input to the polynomial interpolation in the later step. In the present sample, a number of 23 coordinates in a 2D Cartesian coordinate system are detected (Figure 4.6).

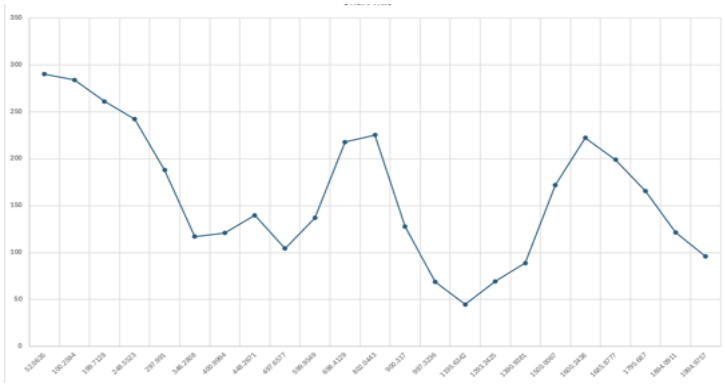

(a) Key points extracted from the original profile.

X	Y	ID
52.0635	290.1644	1
100.2594	284.0719	2
199.7128	261.1592	3
248.5523	242.2604	4
297.991	187.8948	5
346.2808	117.1549	6
400.9994	120.9707	7
448.2671	139.8687	8
497.6577	104.3262	9
599.9549	137.0264	10
698.4129	217.8319	11
802.0443	225.2798	12
900.317	127.7331	13
997.3236	68.795	14
1195.6342	44.8608	15
1293.2425	69.2927	16
1390.9381	88.8224	17
1500.0067	171.9767	18
1600.2438	222.3344	19
1685.8777	199.0211	20
1795.687	165.3996	21
1894.0911	121.5814	22
1994.9757	95.8669	23

(b) Extracted coordinates to represent the bedrock profile and their IDs.

Figure 4.6: Key points extracted from the profile of the buried bedrock, with their coordinates and IDs.

2. Polynomial Interpolation. The curve fitting is developed using the key coordinates of the profile. To reproduce a curve sufficiently similar to the original profile, the a polynomial function of degree equal to 10 is adopted. To this aim, the code listed below had been implemented:

```
import numpy as np

# Loading the extracted coordinates to Python
data = np.loadtxt('coordinate.csv')

# To create a void array for the later coordinate assignment.
coord = np.zeros((23,2))

# Assigning the coordinates value to the void array
for i in range(23):
    coord[i, 0] = data[i, 0]
    coord[i, 1] = data[i, 1]

# To perform the Polynomial Interpolation
degree = 10
coefficients = np.polyfit(coord[:,0], coord[:,1], degree)
polynomial = np.poly1d(coefficients)
x_fit = np.linspace(coord[:,0].min(), coord[:,0].max(), 100)
y_fit = polynomial(x_fit)

polynomial_expression = polynomial
```

Code 4.1: Code to interpolate the bedrock profile

As a result, the polynomial that represents the curve is:

$$y = 9.096 \times 10^{-27}x^{10} - 9.749 \times 10^{-23}x^{9} + 4.461 \times 10^{-19}x^{8} - 1.133 \times 10^{-15}x^{7} + 1.741 \times 10^{-12}x^{6} - 1.648 \times 10^{-9}x^{5} + 9.409 \times 10^{-7}x^{4} - 3.308 \times 10^{-4}x^{3} + 4.937 \times 10^{-2}x^{2} - 3.694x + 384.8 \quad (4.2)$$

The curve is plotted in Figure 4.7.

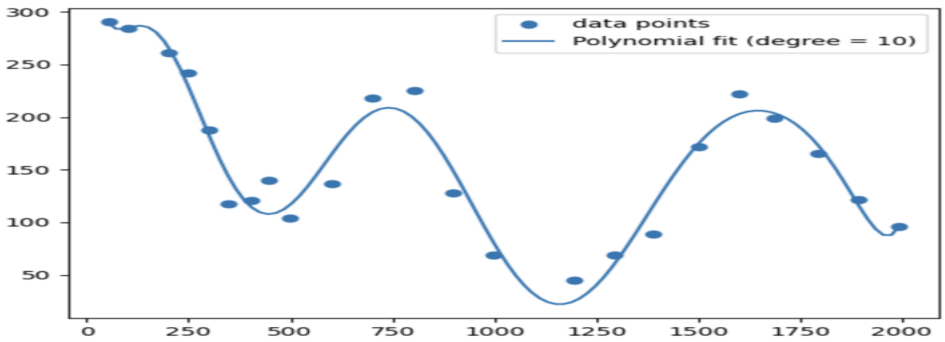

Figure 4.7: The polynomial representation of the buried bedrock.

4.3.2 Hydrostatic and Geological Conditions

According to the dataset available in Holzer and Jachens (1982) [7], the stratigraphic setting of the study area is partly known from the logs of four wells drilled near the boundary of the study area (Figure 2.5) and the behavior of the water table is derived from 11 piezometers located around the margin of the study area (Figure 2.3). These data have been processed as described below to be used in the modeling framework.

Water Level Decline

It is known from wells that the water level was 18 m below the ground surface before it started to decrease about 1940. Thus, the parameter *initial water table* in the model is set to *18*. Since the rate of water level decline was constant until 1962 and the water level itself stabilized at 58 meters below land surface, a linear decline each year with a total lowering equal to 40 m is set. The following is the idea of the specific function that controls the hydrostatic conditions in the simulator.

```
# Define a function for loading the water pressure change

def read_pore_water_pressure_change:
    water_decline = 18

    # Arise Loop to distribute the change of
    # water pressure for every particle points
    for i in range(0, particle_total):

    # Make a statement to determine if that specific
    # point is affected by the changes
    if 0 < depth < 18:
        pressure_change = 0

    else depth_of_bedrock < depth < 18:

        # To make the change become linear
        pressure_change =
        time_step/total_time * water_pressure
```

Code 4.2: Code to define water pressure changes

Under the control of this function, changes in the pressure of the pore water at each depth can be precisely regulated. Specifically, this approach allows for including the following conditions:

1. for soils at depth shallower than 18 m, the water pressures remain constant throughout the simulation. Consequently, the effective stresses for these soils do not change, regardless the step number;

2. for soils located between 18 m below the land surface and the the bedrock boundary, the effective

stress increase linearly over time, corresponding to the progression of the simulation and the decline of the water table.

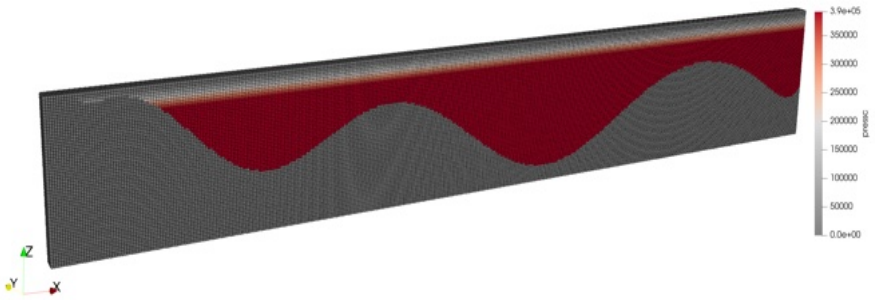

Figure 4.8: Water pressure changes applied to each material point at the end of the simulation period.

Figure 4.8 shows the final water pressure changes at each material point, which are determined by the prescribed lowering of the water table due to groundwater pumping. Points colored blue represent areas with no pressure change throughout the simulation. These points correspond to either the bedrock layer or the unconsolidated alluvium layer located at a depth from the land surface smaller than 18 m. The points colored red represent the portion of the unconsolidated alluvium layer that experienced the most significant changes in water pressure. Meanwhile, points with colors transitioning between red and blue are distributed between depths of -18 m and -58 m, indicating that their pressure changes are proportional to the time step during the simulation.

Soil Layers Setting

As mentioned earlier, the monitored area is divided into two layers: the unconsolidated alluvial layer and the bedrock layer. Although the precise lithology of the material beneath the unconsolidated alluvium in the study area is unknown, it is established that the density contrast between the alluvium and bedrock is 0.5 g/cm^3, based on in-situ gravity measurements.

Furthermore, the density of the bedrock beneath the study area is uniform around the basin margins, with an average value of 2.6 g/cm^3, as determined from density measurements carried out on 15 crystalline bedrock samples. Similarly, the average saturated density of the unconsolidated alluvium is approximately 2.1 g/cm^3, as derived from borehole data.

As no value of the geomechanical properties is available to fully engage the Peridynamics simulation, a trail-and-error approach is employed to estimate Young's modulus, cohesion, and internal friction angle. Initially, the following values have been assigned: $E = 8.3 \times 10^7$ Pa, $c = 1$ kPa, ϕ =30°, and a porosity of 0.3. Accordingly, the two layers, which are unconsolidated alluvium and bedrock, will be characterized by their respective properties and assigned to all material points in the model.

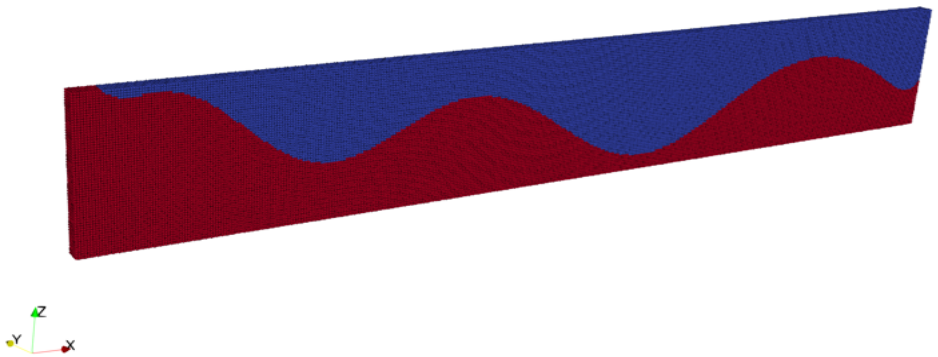

Figure 4.9: The two layers structure applied to each material point

Figure 4.9 illustrates how the two-layer structure is applied to the material points within the model domain. The blue material points represent the upper layer of unconsolidated alluvium, while the red material points correspond to the bedrock layer.

4.3.3 Boundary Conditions

In addition to the hydrostatic and geological conditions, the boundary conditions of the model must be defined to accurately compute the displacements of each material point over time. The boundary conditions in the present model consist of four parts: the first three parts constrain the movement of material points along the X-, Y-, and Z-axes, respectively, while the final part constrains the movement of material points belonging to the bedrock layer.

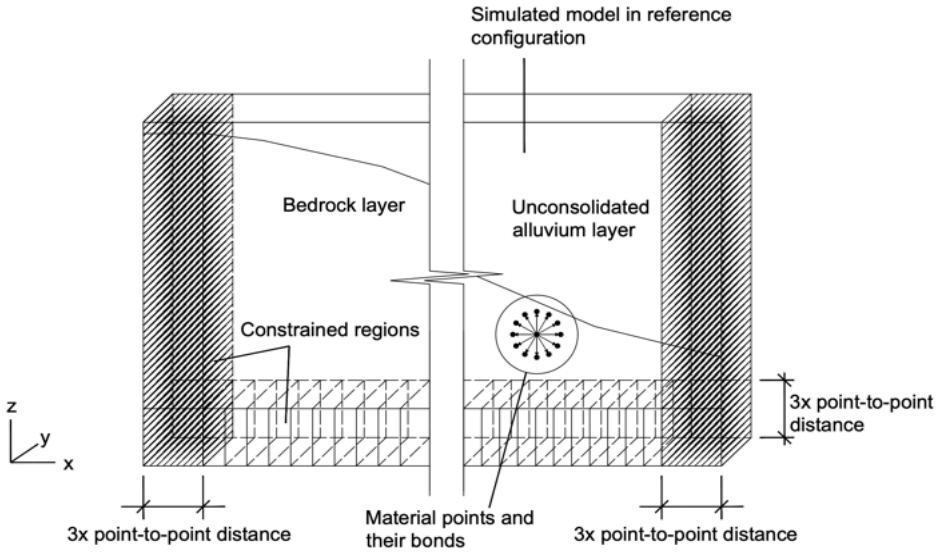

Figure 4.10: Material points in the constrained regions in a 3 dimensional perspective view.

As shown in Figure 4.10, the regions represented by two vertical filled "columns" on either side of the model indicated areas where the movements of material points are restricted along the X-direction. Additionally, the region represented by a horizontal "beam" at the bottom of the model denotes where material points are restricted from moving in any direction. The constraints applied along the Y direction are shown in Figure 4.11. The width of each constrained region is identical to that shown in Figure 4.10, that is, equal to three times the length of the bond between two points of the material.

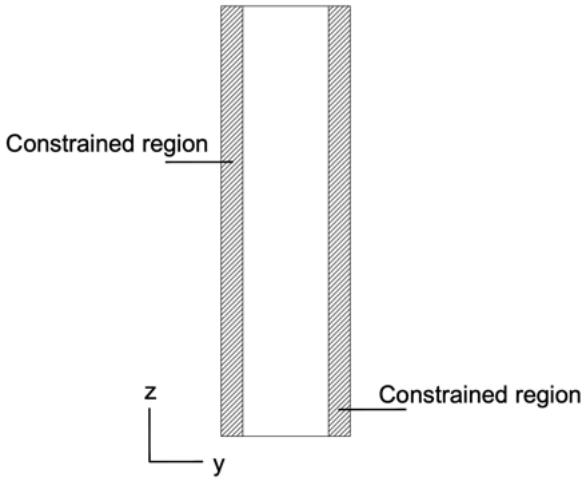

Figure 4.11: Side view of the model where movement precluded along Y direction are shown.

Chapter 5

Results and Discussions

5.1 Peridynamics Validation on the Simple Case Study

A brief comparison of the results provided by the Peridynamics and FEM approaches on the simple case study is crucial to test the validity of the former and to highlight the advantages and limitations of the Peridynamics modeling framework employed in this thesis. This section focuses primarily on the behavior of land subsidence and the development of earth fissures as provided by the modeling results. The aim is to quantify the differences between the two models when subjected to the same initial parameters, providing insights into the relative performance and accuracy of each approach.

5.1.1 Land Subsidence Comparison

In this subsection, the results in terms of land subsidence as computed by Peridynamics and GEPS3D model are shown.

Results from Peridynamics Model

Figure 5.1 shows that the maximum land subsidence calculated from the Peridynamics modeling framework is 0.460 m and develop at the two sides of the rock ridge. The thicker the alluvium layer, the greater is the displacement of the particles alone Z axis.

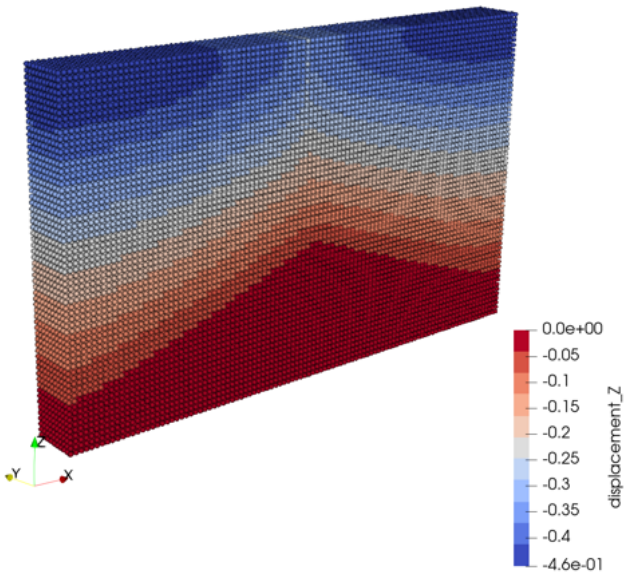

Figure 5.1: Vertical land displacement from Peridynamics modeling approach.

Results from GEPS3D Model

The results in terms of land subsidence as obtained from GEPS3D are shown in Figure 5.2. The maximum land subsidence calculated by GEPS3D is 0.454 m, which is 98.7% the value calculated by the Peridynamics modeling framework.

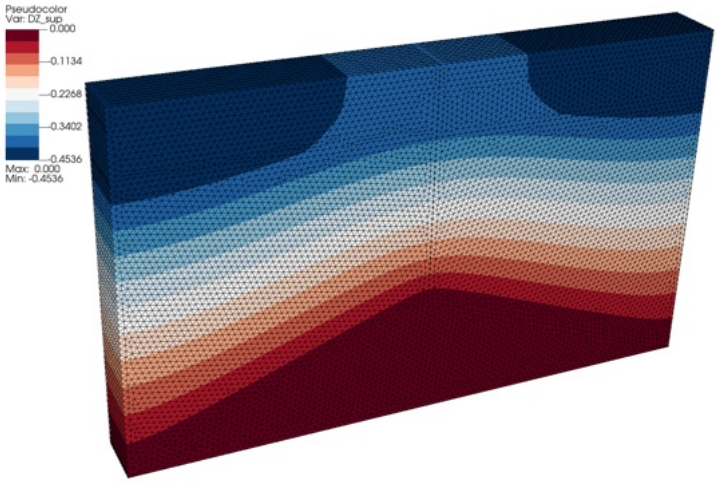

Figure 5.2: Vertical land displacement from GEPS3D.

5.1.2 Earth Fissures Comparison

In this subsection, the results in terms of fissure generation and characteristics are shown as computed by Peridynamics and the GEPS3D model.

Results from Peridynamics Model

The simulated result in terms of the development of the earth fissure is shown in Figure 5.3. The bedrock profile in this model was intentionally designed to include only one inflection point, with the expectation that a single fissure would develop. The results confirm this hypothesis, as only one fissure develops above the tip of the ridge.

Furthermore, the crack pattern aligns with findings from field investigations in the Picacho Basin, which indicated that cracks form in locations where the underlying bedrock profile exhibits maximum concave-upward curvature. The simulation also reveals that the crack initiates at the land surface and gradually propagates downward. The extent of crack development is influenced by the drop in pore water pressure: the greater the decrease in hydrostatic pressure, the deeper the crack propagates.

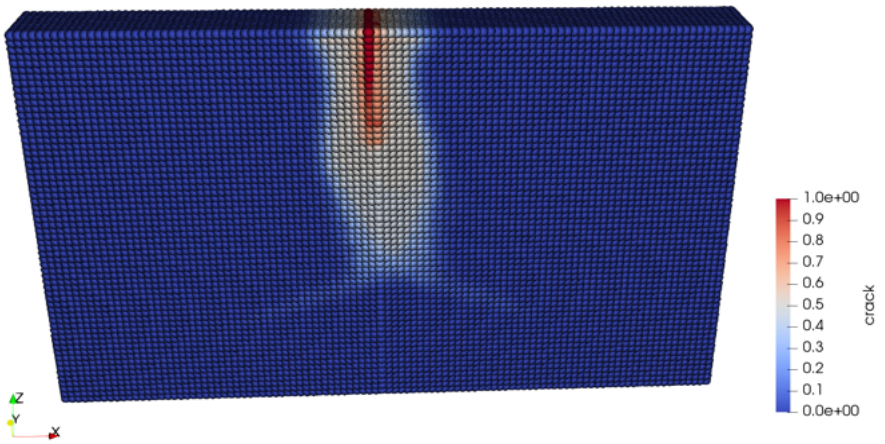

Figure 5.3: Peridynamics modeling result of earth fissure. The red material points, i.e. those with $\Psi > 0.5$ represent the fissure location.

Results from GEPS3D Model

In the case of GEPS3D, the fissure occurrence is evaluated on the behavior of the Interface Elements. The fissure is indicated by the red and green domains in Figure 5.4. This means that the position of the fissure has been correctly predicted.

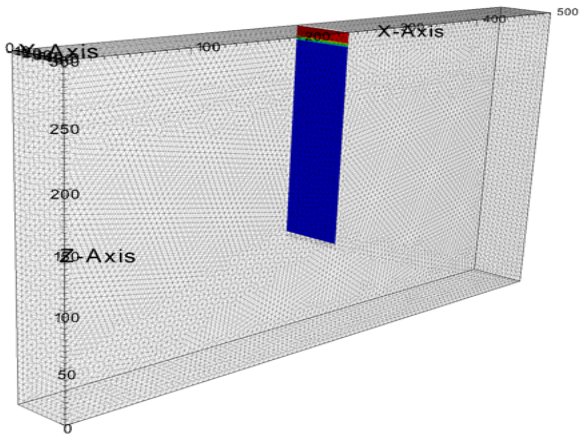

Figure 5.4: Solution of the GEPS3D model on the interface elements: the activated IEs (i.e. the fissure is developed) are colored in red and green, the stuck IEs are colored in blue.

5.1.3 Comparison between Peridynamics and GEPS3D

In summary, the results of the simple case test produced by Peridynamics and the GEPS3D model are very similar. This is particularly evident in terms of land subsidence, where not only the value distributions are nearly identical, but the maximum values differ by less than 2%.

Although it is challenging to precisely quantify the differences in earth fissure development due to the different approach used to represent cracks, their positions and characteristics exhibit similar trends. Both models indicate that a fissure consistently forms above the tip of the buried ridge and propagates from the land surface downward. The fissure results deeper with Peridynamics than with GPS3D.

5.2 Picacho Basin Model Outcomes

This section focuses on the modeling results in terms of land subsidence and earth fissures obtained by Peridynamics in the Pichaco Basin case study. As mentioned above, the total number of time steps is determined manually and can vary significantly depending on the specific case study and the progression of land subsidence and earth fissures in different models. Fissure locations are much more difficult to anticipate in this real case, and consequently, the use of GEPS3D, i.e. a FE-based simulator where IEs must be inserted before running the model, is really challenging.

For the current model, a trial-and-error approach was employed to determine the most efficient number of time steps. To ensure that the entire process of particle movements could be completed, an initial estimate of 1000 steps was chosen. According to the simulation logs, the fissure development appears to stabilize around the 470^{th} time step. Although the process is computationally intensive, a balanced time steps count of **540** steps was selected to optimize both efficiency and accuracy.

Once the initial inputs and the specific time steps are configured, the Peridynamics modeling framework is ready to execute. In the current model, 10 output files are generated after completion of the process, each corresponding to a specific time step. These files contain information on land subsidence and earth fissures, stored in plain text format.

To enable further analysis, the data must first be visualized. For this purpose, the software **Paraview** (Version 5.12) is used as the visualization tool. By applying the built-in *Table to Point* filter, the output results at these 10 time steps are effectively displayed.

Development of the Earth Fissures

One of the biggest advantages of using the non-local Peridynamics model is that the formation of earth fissures can be revealed clearly at any time step without any beforehand interference as those in the FE-IE method. To better illustrate the development of the fissure in the Peridynamics model, a number of 5 out of the 10 printed outputs have been selected, namely the $53^{th}, 215^{th}, 377^{th}, 485^{th}, 539^{th}$ steps. They correspond to a lowering of the water table equal to 4 m, 16 m, 28 m, 36 m and 40 m, respectively.

(a) Percentage of bond break Ψ

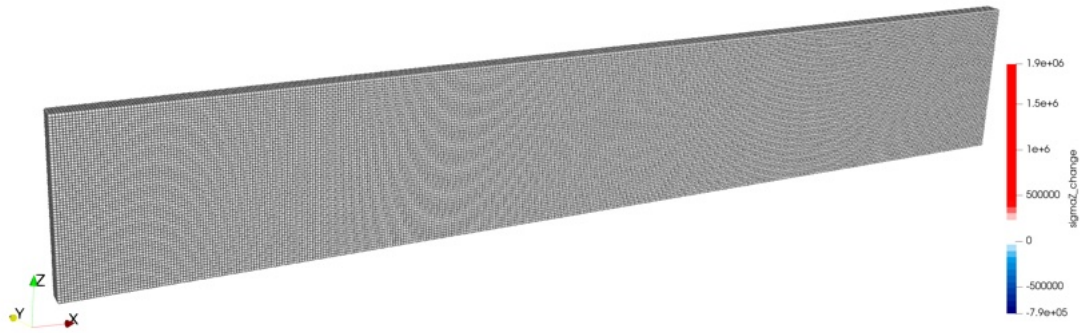

(b) Change of vertical effective stress $\Delta\sigma_z$

Figure 5.5: Peridynamics model outcomes at the 53^{th} time step, corresponding to $\Delta p = 4\ m$.

Figure 5.5a shows the results at the 53^{th} time step. The entire model remains intact, as all material points in this moment are characterized by null damage $\Psi = 0$. To further investigate the effect of the water table decline up to step 53^{th}, we also extracted the map of stress changes along the Z axis (Figure 5.5b), representing the increase of the effective normal stress applied to each particle.

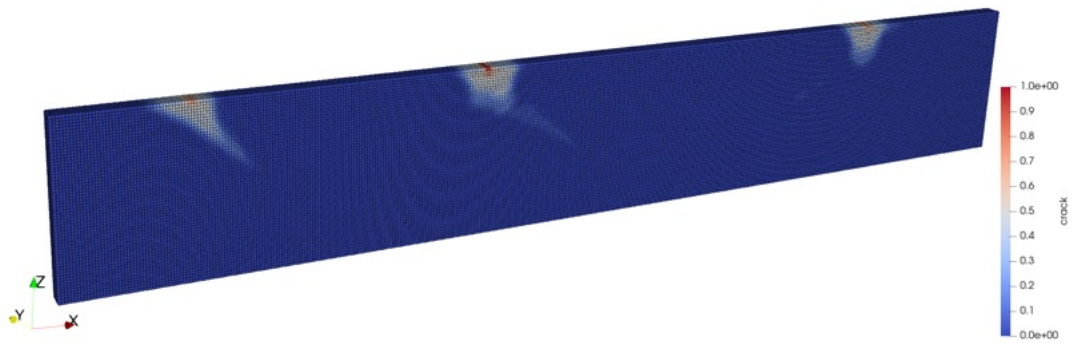

(a) Percentage of bond break Ψ

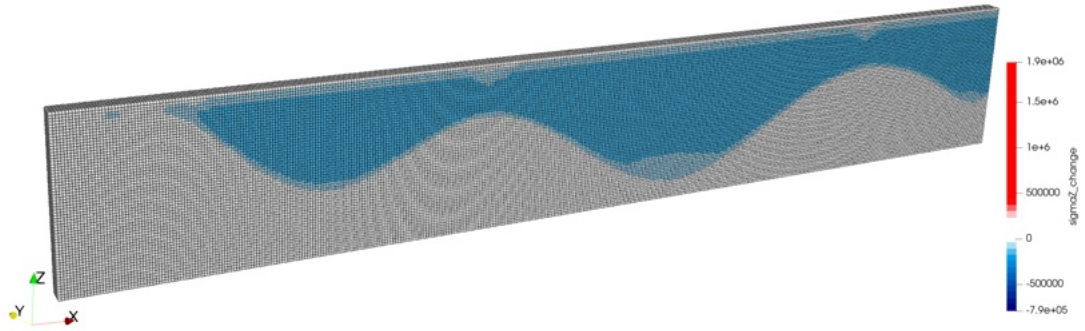

(b) Change of vertical effective stress $\Delta\sigma_z$

Figure 5.6: Peridynamics model outcomes at the 215^{th} time step, corresponding to $\Delta p = 16\ m$.

Figure 5.6a points out that earth fissures start to develop above the two buried bedrock ridges and in proximity of the outcropping rock on the left part of the domain. Figure 5.6b shows the pattern of the effective stress change. The highest values are calculated above the tip of the buried ridges where the fissures develop.

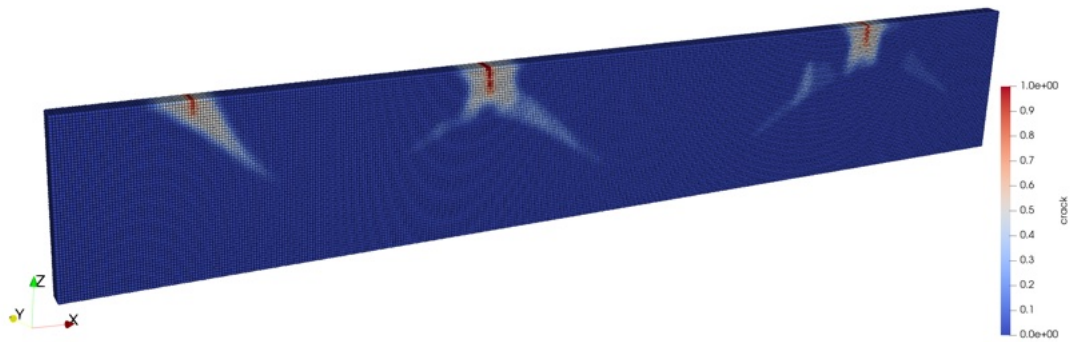

(a) Percentage of bond break Ψ

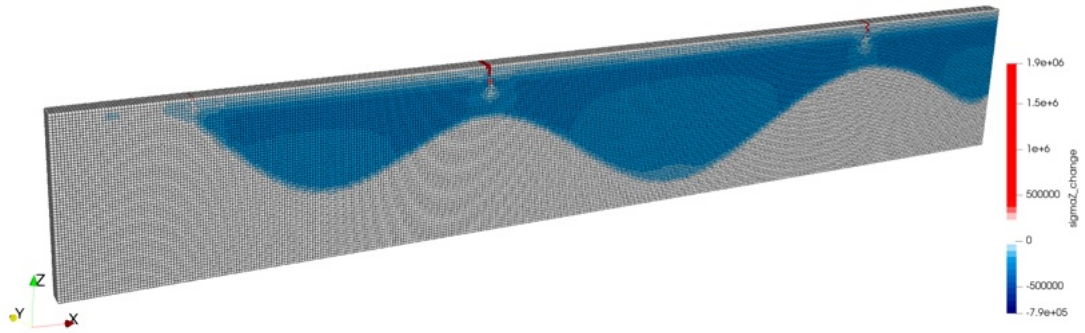

(b) Change of vertical effective stress $\Delta\sigma_z$

Figure 5.7: Peridynamics model outcomes at the 377^{th} time step, corresponding to $\Delta p = 28\ m$.

For the step after the middle of the simulation, that is, the step 377^{th}, the fissures develop further downward, toward the directions of the bedrock profile which has the maximum convex-upward curvature (Figure 5.7a). The corresponding change in vertical effective stress is shown in Figure 5.7b.

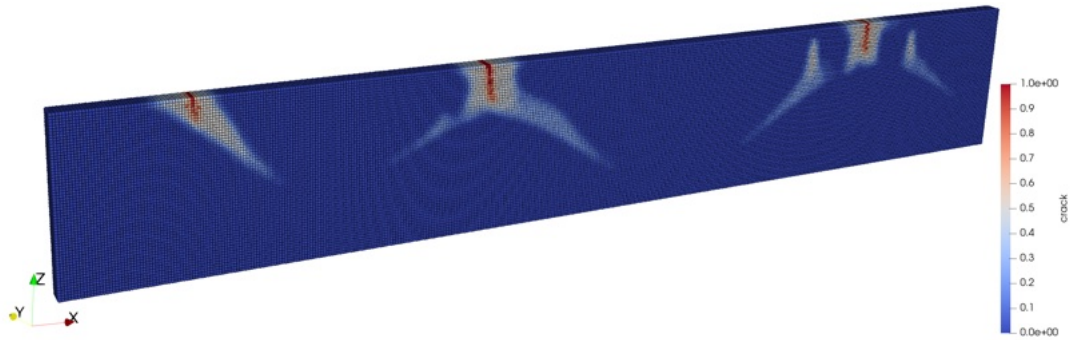

(a) Percentage of bond break Ψ

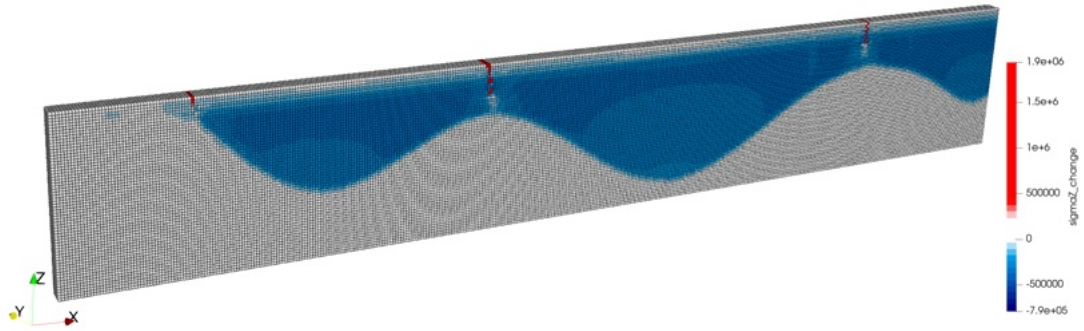

(b) Change of vertical effective stress $\Delta\sigma_z$

Figure 5.8: Peridynamics model outcomes at the 485^{th} time step, corresponding to $\Delta p = 36\ m$.

When the simulation process progresses to the final part in the 485^{th} time step, the model reveals a nearly finished fissure development. Compared with those recorded at the 377^{th} step, the fissures at the 485^{th} step follow the same path of evolution, which vertically goes deeper and approaches the tip of the bedrock profile (Figure 5.8a), indicating that more and more bonds between two material points have been broken due to exceeding their critical stretch (i.e. the red material points in Figure 5.8b).

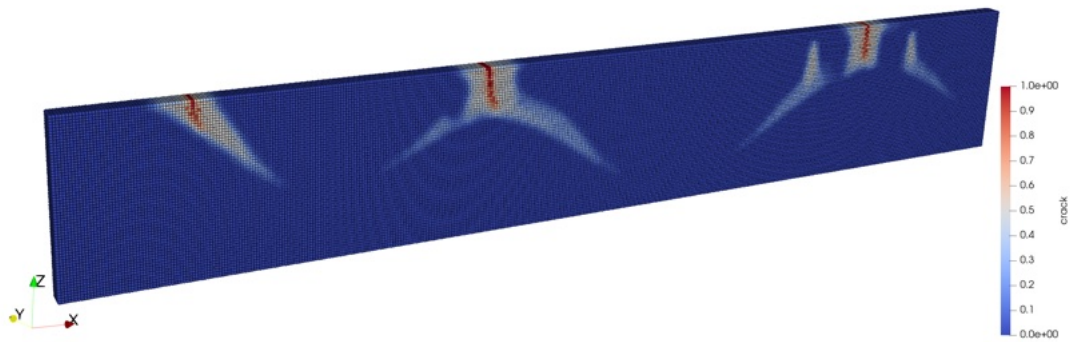

(a) Percentage of bond break Ψ

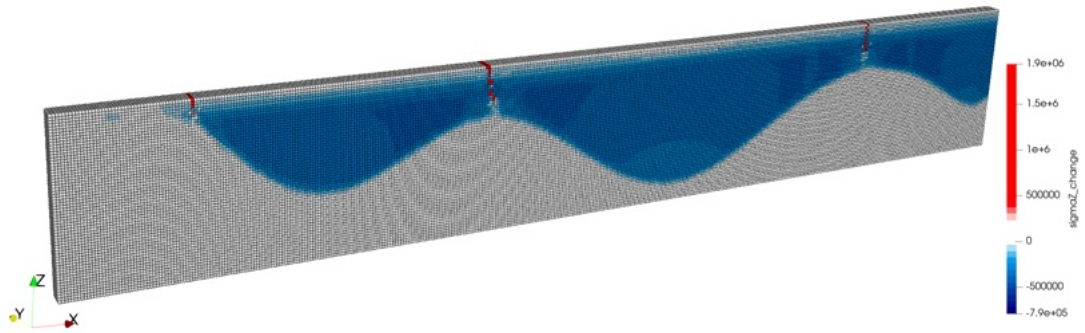

(b) Change of vertical effective stress $\Delta\sigma_z$

Figure 5.9: Peridynamics model outcomes at the 539^{th} time step, corresponding to $\Delta p = 40\ m$.

It is also interesting to investigate the outputs from the last two time steps to confirm whether the particle movements have reached their limit. As shown in Figure 5.9a, the crack development in this step does not exhibit significant variation compared to the 485^{th} time step. Similarly, the stress changes at the final time step show minimal differences in both the distribution pattern and the values compared to those at the 485^{th} step.

Material Points Displacements

The outcomes of the Peridynamics model in terms of displacements of material points along the X and Z axes are presented below in correspondence to the same time steps selected to show the earth fissures.

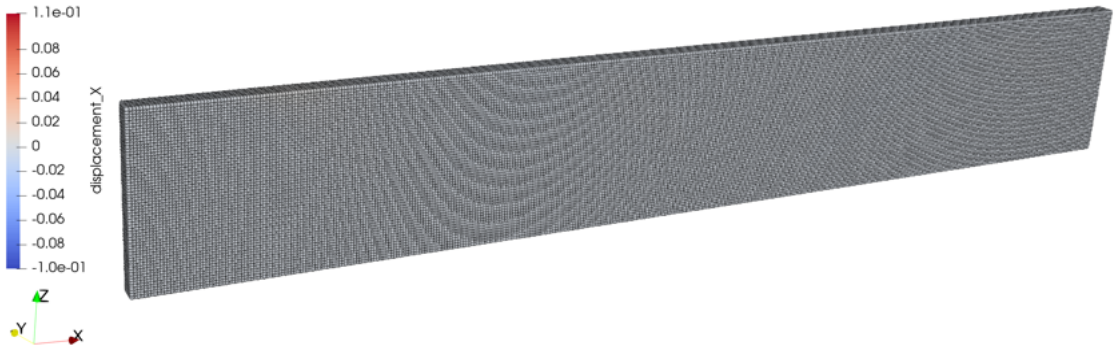

(a) Particle displacements along X axis

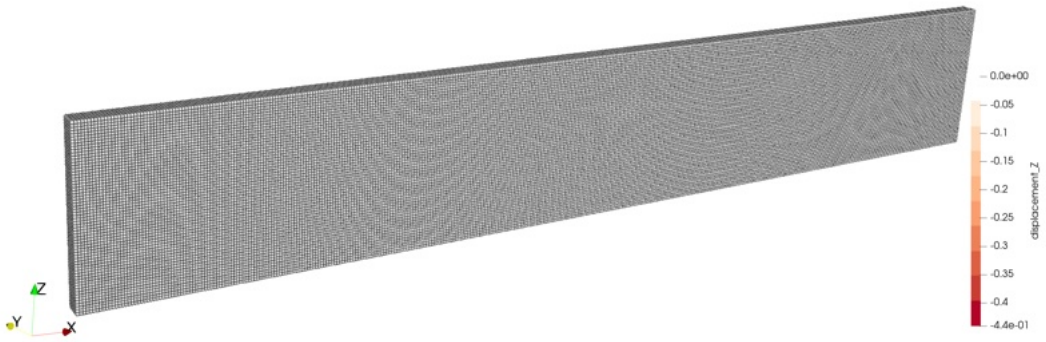

(b) Particle displacements along Z axis

Figure 5.10: Particle displacements at the 53^{th} time step.

As shown in Figure 5.10, the displacements of particles along the X-axis and the Z-axis are negligible at the time step 53^{th}. This is consistent with the outcome in terms of fissure development as shown in Figure 5.5. The 4-m lowering of the water table is too small to cause evident geomechanical consequences.

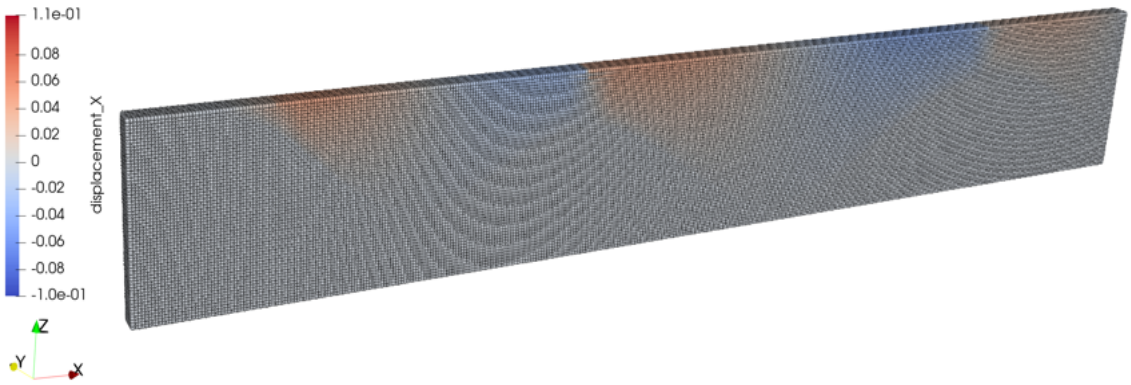

(a) Particle displacements along X axis

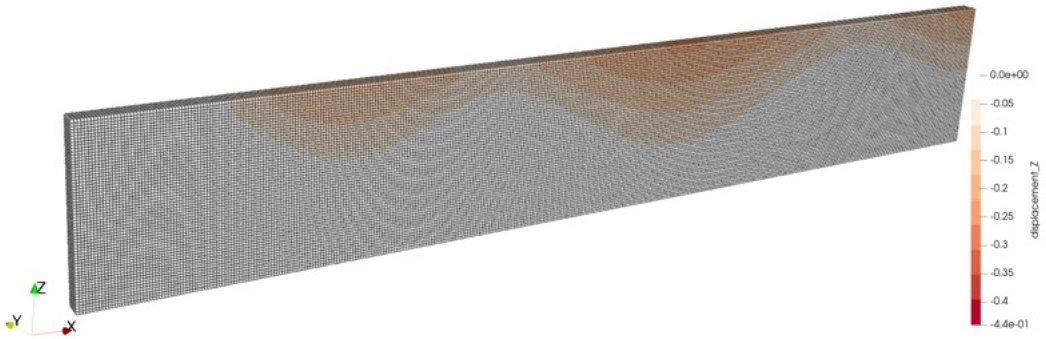

(b) Particle displacements along Z axis

Figure 5.11: Particle displacements at the 215^{th} time step.

The displacements of the material points at the 215^{th} step increase. Since this step on, the links between crack development and the displacements of material point become evident. Figure 5.11a shows that the points above the concave sections of the topographic profile that are convex upward started to move in opposite directions, while in Figure 5.11b, the material points above the concave sections downward of the topographic profiles experienced the greatest displacement along the Z axis.

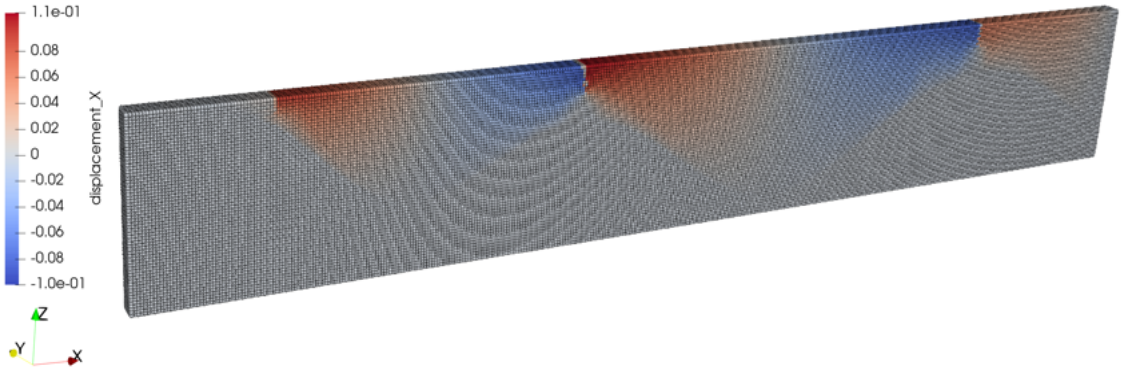

(a) Particle displacements along X axis

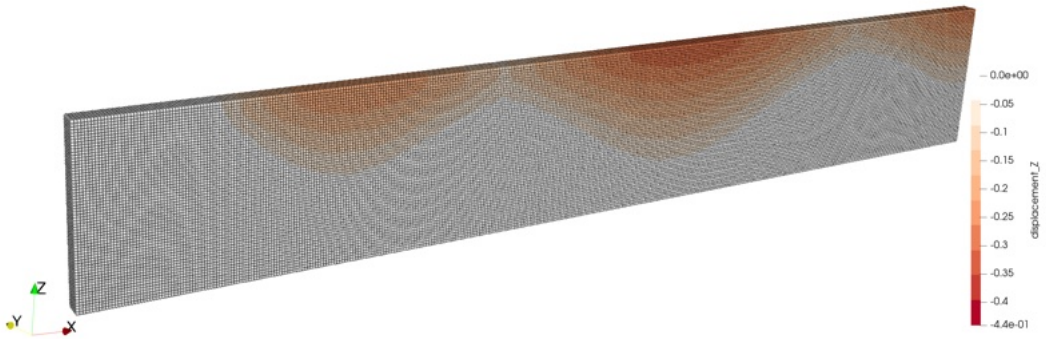

(b) Particle displacements along Z axis

Figure 5.12: Particle displacements at the 377^{th} time step.

When the time comes to step 377^{th}, the horizontal displacements of the material points in Figure 5.12a have become so large that the first crack finally developed in the middle. At the same time, the vertical displacements above the concave-downward topographic profile became larger than other places in the model.

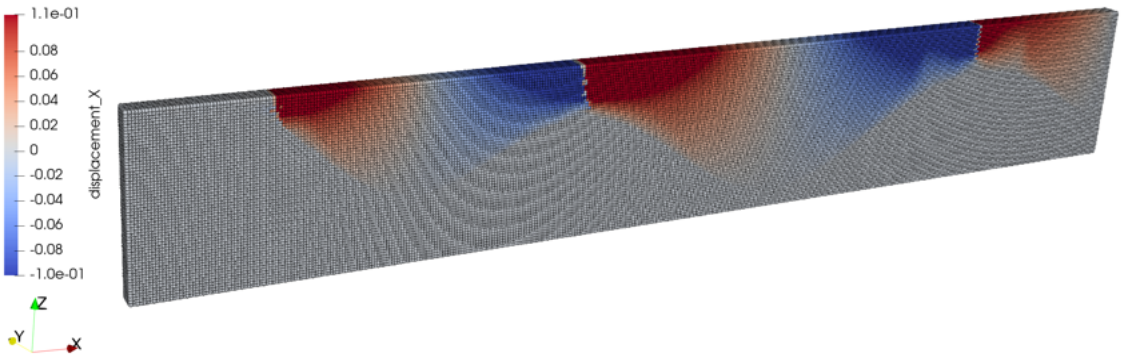

(a) Particle displacements along X axis

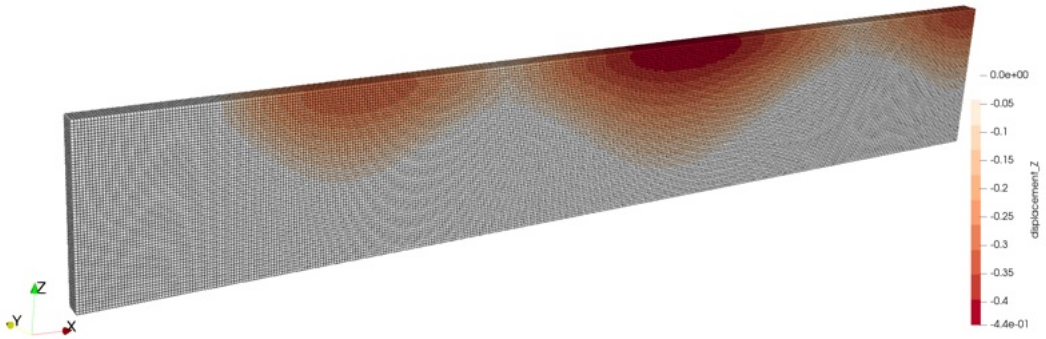

(b) Particle displacements along Z axis

Figure 5.13: Particle displacements at the 539^{th} time step.

In the final step of the simulation, the particle displacements continue to expand in both the X and Z axes. The largest negative displacement along the Z equals 0.442 m. In the unconsolidated alluvium layer, the locations above the concave-downward topographic profile continue to experience the largest displacement along the Z direction while the points above the convex-upward profiles experience the least vertical displacements. The material points representing the bedrock layer show no displacement in all direction during the whole simulation process. In summary, the distribution of vertical displacements shows a strong relation with the thickness of the unconsolidated alluvial layer and the behavior of profiles under this layer in the model.

5.3 Comparisons Between Computational Results and Field Investigation

A practical method to verify the validity of the results produced by the Peridynamics model is to compare them with field observations and previously recorded data. Since the goal is to develop a model that objectively reflects real-world conditions and reconstructs a scenario practical enough for application, the calculated displacements along the z-axis will be compared with the recorded land subsidence in the Picacho Basin study area. Similarly, the crack development simulated by the model will be evaluated against the observed earth fissures from the same study area.

Land Subsidence Comparison

According to site investigations by Holzer and Jachens (1982) [7], the maximum land subsidence was measured on the southeastern side of Mount Casa Grande, reaching a value of 0.79 m in 1980. However, the location of this benchmark is quite far from the area addressed by the modeling analyses. Instead, based on the information provided in Figure 2.6, we have redrawn the zone of earth fissures to highlight the position of the section addressed by the model and the nearest benchmark to monitor land subsidence (Figure 5.14).

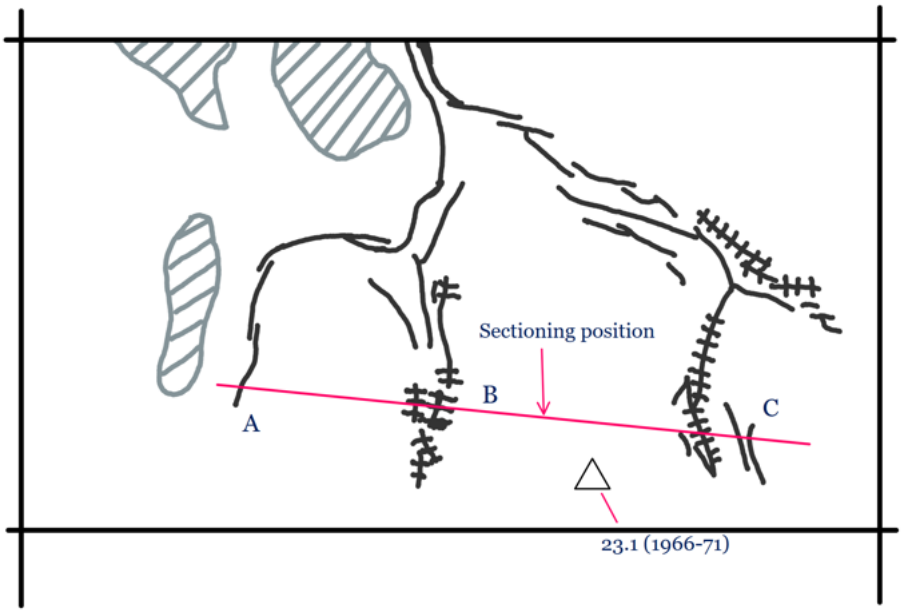

Figure 5.14: Trace of the simulated profile with the location of the earth fissures and the measured land subsidence.

Figure 5.14 shows that land subsidence between fissure zones B and C amounted to 23.1 cm in 1966. Based on the date reported in Chapter 2, which indicated that land subsidence in 1966 accounted for only 49% of the total subsidence by 1980, the final maximum land subsidence in this region is estimated at 47.1 cm.

Given that the soil properties in the Picacho Basin are unknown, several key parameters including cohesion, internal friction angle, and Young's modulus were initially assumed from bibliographic information. In the first computational results generated by the Peridynamics model, the maximum land subsidence was calculated as 77 cm, occurring between zones B and C. Although the location of this maximum value aligned with field observations, the magnitude of land subsidence differs by a factor approximately equal to 2 from the measurements, indicating inaccuracies in the assumed parameters.

A comparison of earth fissure behavior between this initial model and field observations revealed an excellent match, suggesting that the primary issue lay in the parameter assumptions for subsidence modeling. To refine the model and ensure more realistic physical conditions, Young's modulus was

adjusted. Through a trial and error process, Young's modulus in the Peridynamics model was revised from the initial 8.33×10^7 Pa value to 1.5×10^8 Pa.

As demonstrated in Section 5.2, after modifying Young's modulus, the maximum land subsidence predicted by the model between zones B and C was 44.2 cm, in good agreement with the measurements. The difference between the measured and computed land subsidence reduces to approximately 6% compared to the corresponding value of the case study.

Earth Fissures Comparison

From the surface topography observed in April 1980 (Figure 4.4), all the earth fissures in this area are located in correspondence of the buried bedrock ridges. The number and distribution of cracks in the calculated model follow the same pattern as those observed in the study area.

5.4 Discussion

The mechanisms of land subsidence and earth fissures in the study area were thoroughly investigated by Holzer and Jachens (1982)[7]. Their study demonstrated that differential vertical subsidence along the same horizontal layer is the primary factor responsible for generating differential horizontal strains at the land surface. These strain variations result in horizontal tensile stresses that, when exceeding the maximum tensile strength of the soil layer, lead to tensile failure and, consequently, to the formation of earth fissures.

Although the phenomena of land subsidence and earth fissures observed in the Picacho Basin closely resemble the results calculated using the non-local Peridynamics model, it is essential to establish the logical causation behind these outcomes rather than attributing them to coincidence. By clarifying the underlying reasons for these results, we can further validate the effectiveness of the current algorithm based on the newly constructed Peridynamics theory. This, in turn, supports the model's potential for application to other real-world case studies.

As mentioned in the previous sections, the study area is represented by several thousand discrete material points. The motion of these points is governed by a constitutive relationship embedded within the source code of the model. To better illustrate this process, consider a randomly selected material point located within the unconsolidated alluvium layer and below the initial water table.

Since the model is programmed to simulate a gradual decline in the water table, a corresponding change in pore pressure is generated at this point. This change in pressure, in turn, serves as the new input for the so-called peridynamic pressure p.According to the equation proposed by Silling (2007), the peridynamic force $\underline{t}$, under the assumption of an isotropic linear peridynamic solid, can be calculated as:

$$\underline{t} = \frac{-3p}{m}\underline{\omega x} + \alpha\underline{\omega e^d} \tag{5.1}$$

where $\underline{\omega}$ is the influence function, $\underline{x}$ is the relative distance between this random point and its family point, and $\underline{e^d}$ is the deviatoric part of extension.

For each material point in the model, whenever changes in water pressure occur, the corresponding peridynamic forces are computed following the same process. Collectively, these peridynamic forces form the *force vector state field*, as described in Equation 3.10. The displacements of the material points due to the water table decline are then solved iteratively.

However, since the Peridynamics equation employs explicit time integration while the current simulation is performed under quasi-static conditions, an *adaptive dynamic relaxation* method is applied to achieve a steady-state solution. The present code implements the theory proposed by Kilic and Madenci (2010) [21], reformulating Equation 3.10 into a system of ordinary differential equations. This approach establishes the relationship between displacement $\mathbf{U}$, velocity $\dot{\mathbf{U}}$, acceleration $\ddot{\mathbf{U}}$ and peridynamic force $\mathbf{F}$ at the collocation points, expressed as:

$$\mathbf{\Lambda}\ddot{\mathbf{U}}(\mathbf{X},t) + c\mathbf{\Lambda}\dot{\mathbf{U}}(\mathbf{X},t) = \mathbf{F}(\mathbf{U},\mathbf{U}',\mathbf{X},\mathbf{X}') \tag{5.2}$$

where

- $\mathbf{\Lambda}$ is the fictitious diagonal density matrix and by Greschgorin's theorem, its eigenvalue is defined as

$$\lambda_{ii} \geq \frac{1}{4}\Delta t^2 \sum_j |K_{ij}|$$

- c_n is the damping coefficient and is defined as

$$c_n = 2\sqrt{((U^n)^{T\,1} K^n U^n)/((U^n)^T U^n)}$$

With the time step size set to 1, the new displacements for all material points due to the water table decline are calculated and updated at each time step in a dedicated matrix, referred to as the displacement matrix. By superimposing this matrix onto another matrix that stores the coordinate information, it becomes possible to compute both the bond lengths for the collocation points in the reference configuration and the deformation configuration. Additionally, the land subsidence at each time step can be determined, as it corresponds to the displacement along the z-axis.

At this stage, the model proceeds to determine the formation of earth fissures, as the deformation gradient tensor for the entire field has already been generated using Equation 3.14. By linking the deformation gradient tensor with the strain tensor through Equation 3.15, the stress tensor for each material point is updated at each time step based on the prescribed constitutive relation in Equation 3.18.

With the stress tensor calculated, it is compared against the soil's shear strength as defined in the previous section. Following the conventions of soil mechanics, the unconsolidated alluvium layer is assumed to have no tensile strength. Thus, a bond is labeled as cracked in the program if either of the following conditions is met:

1. The shear stress at a collocation point exceeds the shear strength of the soil, or

2. The bond stress at a collocation point is greater than or equal to zero.

When a bond is labeled as cracked, it is removed from subsequent time steps by excluding its contribution to structural support in the model. The degree of damage is then determined by calculating the proportion of cracked bonds within the material point's horizon. This damage metric represents the extent of earth fissures generated in the model.

Finally, the simulator provides the results of the simulated land subsidence and earth fissures after completing the designated 540 time steps. Based on the underlying logic embedded in the code, it can be concluded that the alignment between the simulated results from the Peridynamics-based non-local model and the observations at the Picacho Basin is strongly supported by substantial evidence. This consistency reinforces the validity of the Peridynamics approach for modeling such geomechanical phenomena.

Chapter 6

Conclusions

The traditional Finite Element Method (FEM), grounded in continuum theory, has long served as a fundamental tool for analyzing how changes in the water table within an aquifer affect soil behavior. However, FEM has demonstrated significant limitations in simulating earth fissures, which are critical for accurate geohazard prediction. Consequently, there is a pressing need to explore alternative approaches to address these challenges effectively.

This thesis adopts a novel modeling framework developed by Ye et al. (2024) [4] based on the Peridynamics theory, to address the limitations observed in traditional methods. The primary focus of the thesis are: i) To investigate the capability of the Peridynamics modeling framework and its applicability in the field of geomechanics; ii) To apply the methodology for the simulation of the continuous (land movements) and discontinuous (earth fissures) deformation patterns associated to over-exploitation of complex phreatic and confined aquifer systems.

To illustrate the first objective, two simple models constructed using the Finite Element Method (FEM) and the Peridynamics modeling framework were examined, respectively. By assigning identical soil mechanical properties and loads to both models, the reliability and accuracy of the Peridynamics modeling framework in predicting land subsidence were confirmed through direct comparisons with FEM results. These comparisons also facilitated a detailed analysis of the strengths and weaknesses of the Peridynamics approach. The advantages of Peridynamics, as revealed through this study, are particularly notable:

1. One of the most significant advantages of Peridynamics lies in its inherent ability to model crack development without the need for pre-defined crack locations or additional insertions. Unlike the Finite Element Method (FEM), which requires the prediction of crack positions and the insertion of interface elements (IE) to enable mesh divisibility, Peridynamics employs integral equations. This eliminates the issue of non-differentiability along the fissure plane, allowing the material points within the model to move freely. As a result, the Peridynamics framework produces earth fissure that are more representative of real-world scenarios, as it avoids the manual prediction step inherent to FEM. This step in FEM can introduce deviations and reduce the accuracy of the simulation, whereas Peridynamics naturally accommodates the spontaneous development of the fissures.

2. The lines of code required to define the same set of model conditions such as dimensions, layer properties, and load changes are significantly fewer in the Peridynamics framework compared to the Finite Element Method (FEM). This reduction in code complexity results in a lighter key file for the simulator. Consequently, developers can spend less time on model construction, thereby enhancing productivity from this perspective.

3. With fewer lines of code in the Peridynamics framework, it becomes possible to adjust a single parameter while allowing other dependent parameters to update automatically. For instance, in the Finite Element Method (FEM), increasing the mesh density to improve result accuracy typically requires rebuilding the entire mesh, redistributing the coordinate system, and redefining the element system from scratch. In contrast, Peridynamics achieves the same effect by simply adjusting

the parameter governing the distance between two material points, without the need for changes to other components. This streamlined approach significantly reduces the complexity and time required for model modifications.

On the other hand, the newly developed Peridynamics modeling framework is not without its limitations, which stem partly from the inherent nature of the framework and partly from the choice of programming language used for its implementation (i.e., Python):

1. The Peridynamics model consists of a large number of material points, each separated by a fixed distance in all directions. As a result, it becomes challenging to accurately replicate the exact shapes of highly irregular subsurface layers. Additionally, the method for distinguishing different interfaces within the model is currently limited to polynomial representations. If the interface between two layers is a complex curve with numerous inflection points, it becomes exceedingly difficult to mathematically express this curve within the model. Fortunately, this limitation can be partially mitigated by increasing the degree of the polynomial used to approximate the interface.

2. If the model to be constructed spans a large spatial scale, a significant amount of physical RAM is required so much so that handling such a model would have been impractical even on high-performance computers. This highlights that the computational cost of the Peridynamics framework is an order of magnitude higher than that of the Finite Element Method. However, advances in computer manufacturing technology have made it possible to manage relatively large-scale models using modern server-level computers, mitigating this limitation to some extent.

The second objective addresses the applicability of the Peridynamics modeling framework to various types of phreatic and confined aquifer structures. We constructed a model measuring 2000 m in width and 300 m in depth, based on a segment of the Picacho Basin area. The results of this model demonstrated a high degree of similarity to field observations, both in terms of land subsidence and earth fissures. Specifically, the accuracy of the land subsidence simulation was within 6% of the observed values, while the locations and quantities of earth fissures matched the field data precisely. These minimal differences strongly validate the successful application of the Peridynamics modeling framework to phreatic aquifer systems. Moreover, the findings underscore the potential of this method to expand its applicability to a wider range of aquifer systems, positioning it as a promising tool for advancing future geomechanical studies.

In conclusion, the newly developed Peridynamics modeling framework has proven to be highly capable in predicting land subsidence and exceptionally effective in simulating earth fissures. This represents a significant advance in the treatment of geohazards, which pose threats not only to infrastructure but also to human life. Given its demonstrated reliability and potential, the Peridynamics model is a valuable tool that merits further promotion and application in geomechanical studies and hazard prevention efforts.

Bibliography

[1] Hasanuddin Z. Abidin, Heri Andreas, Irwan Gumilar, Yoichi Fukuda, Yusuf E. Pohan, and T. Deguchi. Land subsidence of jakarta (indonesia) and its relation with urban development. *Natural Hazards*, 59(3):1753–1771, 2011.

[2] GY Wang, G You, B Shi, ZL Qiu, HY Li, and M Tuck. Earth fissures in jiangsu province, china and geological investigation of hetang earth fissure. *Environmental Earth Sciences*, 60:35–43, 2010.

[3] Hisao Hirai, Hiroshi Kubo, Mutsuo Yamaya, Katsutoshi Nakayama, Muneo Numasaki, Seiichi Kobayashi, Satoshi Suzuki, Shigeki Shibahara, and Hidetada Sasaki. Microsatellite polymorphism in heme oxygenase-1 gene promoter is associated with susceptibility to oxidant-induced apoptosis in lymphoblastoid cell lines. *Blood*, 102(5):1619–1621, 2003.

[4] Miao Ye, Lin Zhu, Andrea Franceschini, Jiangtao Li, Huili Gong, Xiaojuan Li, and Pietro Teatini. Peridynamics modelling of multi-fissure occurrence in the north china plain aquifer system. *Water Resouces Research*, Submitted, 2024.

[5] S. A. Silling, M. Epton, O. Weckner, J. Xu, and E. Askari. Peridynamic states and constitutive modeling. *Journal of Elasticity*, 88(2):151–184, 2007.

[6] Stewart A Silling. Reformulation of elasticity theory for discontinuities and long-range forces. *Journal of the Mechanics and Physics of Solids*, 48(1):175–209, 2000.

[7] Robert C Jachens and Thomas L Holzer. Differential compaction mechanism for earth fissures near casa grande, arizona. *Geological Society of America Bulletin*, 93(10):998–1012, 1982.

[8] DR Pool. Variations in climate and ephemeral channel recharge in southeastern arizona, united states. *Water resources research*, 41(11), 2005.

[9] RJ Szymber and WD Sellers. Atmospheric turbidity at tucson, arizona, 1956–83: Variations and their causes. *Journal of Applied Meteorology and Climatology*, 24(7):725–734, 1985.

[10] Karl Terzaghi, Ralph B Peck, and Gholamreza Mesri. *Soil mechanics in engineering practice*. John wiley & sons, 1996.

[11] Thomas L Holzer. Ground failure induced by ground-water withdrawal from unconsolidated sediment. *Reviews in engineering geology*, 6:67–106, 1984.

[12] Phillip Anderson. Proterozoic plate tectonic evolution of arizona. *Geologic evolution of Arizona: Arizona Geological Society Digest*, 17:17–55, 1989.

[13] BE Lofgren. Hydraulic stresses cause ground movement and fissures, picacho, arizona. *Geological Society American Abstracts Programs*, 10(3):113, 1978.

[14] Donald C Helm. Hydraulic forces that play a role in generating fissures at depth. *Bulletin of the Association of Engineering Geologists*, 31(3):293–304, 1994.

[15] Thomas L Holzer, Stanley N Davis, and Ben E Lofgren. Faulting caused by groundwater extraction in southcentral arizona. *Journal of Geophysical Research: Solid Earth*, 84(B2):603–612, 1979.

[16] Muniram Budhu. Mechanics of earth fissures using the Mohr-Coulomb failure criterion. *Environmental & Engineering Geoscience*, 14(4):281–295, 2008.

[17] M. A. Biot. General theory of three-dimensional consolidation. *Journal of Applied Physics*, 12(2):155–164, 1941.

[18] Shujun Ye, Andrea Franceschini, Yan Zhang, Carlo Janna, Xulong Gong, Jun Yu, and Pietro Teatini. A novel approach to model earth fissure caused by extensive aquifer exploitation and its application to the Wuxi case, China. *Water Resources Research*, 54(3):2249–2269, 2018.

[19] Matteo Frigo, Massimiliano Ferronato, Jun Yu, Shujun Ye, Devin Galloway, Dora Carreón-Freyre, and Pietro Teatini. A parametric numerical analysis of factors controlling ground ruptures caused by groundwater pumping. *Water Resources Research*, 55(11):9500–9518, 2019.

[20] Yueting Li, Pietro Teatini, Jun Yu, Andrea Franceschini, Matteo Frigo, Claudia Zoccarato, and Shujun Ye. Aseismic multifissure modeling in unfaulted heavily pumped basins: Mechanisms and applications. *Water Resources Research*, 57(10):e2021WR030127, 2021.

[21] Bahattin Kilic and Erdogan Madenci. An adaptive dynamic relaxation method for quasi-static simulations using the peridynamic theory. *Theoretical and Applied Fracture Mechanics*, 53(3):194–204, 2010.